

Accepted for ApJ, Vol 738 (Sept. 1, 2011)

Hubble-COS Observations of Galactic High-Velocity Clouds: Four AGN Sight Lines through Complex C¹

J. Michael Shull, Matthew Stevans, Charles Danforth, Steven V. Penton
CASA, Department of Astrophysical and Planetary Sciences, University of Colorado,
389-UCB, Boulder, CO 80309

Felix J. Lockman, National Radio Astronomy Observatory, Green Bank, WV 29444;
Nahum Arav, Department of Physics, Virginia Tech, Blacksburg, VA 24061

michael.shull@colorado.edu, matthew.stevans@colorado.edu,
charles.danforth@colorado.edu, steven.penton@colorado.edu,
jlockman@nrao.edu, arav@vt.edu

ABSTRACT

We report ultraviolet spectra of Galactic high-velocity clouds (HVCs) in Complex C, taken by the Cosmic Origins Spectrograph (COS) on the *Hubble Space Telescope* (*HST*), together with new 21-cm spectra from the Green Bank Telescope. The wide spectral coverage and higher S/N, compared to previous HST spectra, provide better velocity definition of the HVC absorption, additional ionization species (including high ions), and improved abundances in this halo gas. Complex C has a metallicity of 10–30% solar and a wide range of ions, suggesting dynamical and thermal interactions with hot gas in the Galactic halo. Spectra in the COS medium-resolution G130M (1133–1468 Å) and G160M (1383–1796 Å) gratings detect ultraviolet absorption lines from 8 elements in low ionization stages (O I, N I, C II, S II, Si II, Al II, Fe II, P II) and 3 elements in intermediate and high-ionization states (Si III, Si IV, C IV, N V). Our four AGN sight lines toward Mrk 817, Mrk 290, Mrk 876, and PG 1259+593 have high-velocity H I and O VI column densities, $\log N_{\text{HI}} = 19.39\text{--}20.05$ and $\log N_{\text{OVI}} = 13.58\text{--}14.10$, with substantial amounts of kinematically associated photoionized gas. The high-ion abundance ratios are consistent with cooling interfaces between photoionized and collisionally ionized gas: $N(\text{C IV})/N(\text{O VI}) \approx 0.3\text{--}0.5$, $N(\text{Si IV})/N(\text{O VI}) \approx 0.05\text{--}0.11$, $N(\text{N V})/N(\text{O VI}) \approx 0.07\text{--}0.13$, and $N(\text{Si IV})/N(\text{Si III}) \approx 0.2$.

Subject headings: Galaxy: halo — ISM: clouds — ultraviolet: general

1. Introduction

Absorption spectra in the ultraviolet (UV) provide sensitive diagnostics of conditions in the halo of the Milky Way, where competing process of accretion and outflow determine the evolution of the Galaxy. Recent measurements (Shull et al. 2009) provide considerable insight into the infall of low-metallicity gas onto the disk, an ongoing process that can account for the observed stellar metallicities, star formation rates, and mass-metallicity relations (Pagel 1994; Gilmore 2001; Tremonti et al. 2004). Galactic high-velocity H I clouds (HVCs) are plausible candidates for this fresh material. However, as long as they were only observed in the 21 cm line, their overall properties remained somewhat obscure. In recent years, sensitive UV and optical spectroscopy have revitalized this field, providing metallicities (10–20% solar) and reliable distance measurements to several prominent clouds such as Complex C, Complex M, and the Magellanic Stream.

The infall of low-metallicity gas onto the Milky Way is a crucial component of most models of Galactic formation and evolution (Gibson et al. 2001) required to explain the metallicity distribution of nearby G- and K-dwarfs, the so-called “G-dwarf problem” (Pagel 1994). Infall models are attractive because Galactic disk formation is believed to occur by the gradual accretion of pristine or partially processed material into the interstellar medium (ISM). The metallicity of the initial reservoir of gas is enriched by ejecta from star formation and mixing with infalling low-metallicity gas, possibly through “cold-mode accretion” (Dekel & Birnboim 2006; Kereš et al. 2009). This process continues to the present day, regulated in a manner that produces the local G-dwarf metallicity distribution and avoids the overproduction of metal-poor disk stars. The infall of gas from the intergalactic medium (IGM) and low Galactic halo also places a chemical imprint on mass–metallicity relations (Erb et al. 2006).

One likely manifestation of infall from the halo into the disk may have been observed in the system of Galactic high-velocity clouds (HVCs). These HVCs were defined as neutral hydrogen clouds moving at velocities incompatible with differential Galactic rotation (Wakker & van Woerden 1997). First discovered in 21-cm emission, Galactic HVCs have become even more interesting when observed in UV absorption lines of heavy elements (Wakker et al. 1999; Gibson et al. 2000, 2001; Richter et al. 2001; Sembach et al. 1999, 2003; Collins, Shull, & Giroux 2003, 2004, 2005, 2007, 2009; Fox et al. 2004, 2006). Hereafter, we denote the Collins et al. papers as CSG03, CSG07, CSG09, etc. The UV data also demonstrate

¹Based on observations made with the NASA/ESA *Hubble Space Telescope*, obtained from the data archive at the Space Telescope Science Institute. STScI is operated by the Association of Universities for Research in Astronomy, Inc. under NASA contract NAS5-26555.

that HVCs are more extended on the sky at lower total hydrogen column densities. Their “extended atmospheres” often contain more ionized gas than neutral gas, as seen in their $H\alpha$ emission (Tufte, Reynolds, & Haffner 1998).

The UV absorption-line surveys find that a greater fraction of the high-latitude sky is covered with infalling ionized gas than would have been suspected from 21 cm data. In 21-cm emission, the HVC sky-covering factor is 37% down to column densities $N_{\text{HI}} \gtrsim 8 \times 10^{17} \text{ cm}^{-2}$ at the 4σ level (Lockman et al. 2002). In surveys using the more sensitive UV absorption lines, the sky coverage is much higher: $\gtrsim 60\%$ in O VI $\lambda 1031.9$ (Sembach et al. 2003) and $81 \pm 5\%$ in Si III $\lambda 1206.5$ (Shull et al. 2009). Owing to its large oscillator strength, the Si III absorption line is the best probe of ionized HVCs, typically 4–5 times stronger than O VI. From our *HST*/STIS survey of high-velocity Si III (Shull et al. 2009; CSG09), we infer that the low Galactic halo is enveloped by a sheath of ionized, low-metallicity gas, which can provide a substantial cooling inflow ($\sim 1 M_{\odot} \text{ yr}^{-1}$) to help replenish star formation in the Galactic disk, estimated at $2\text{--}4 M_{\odot} \text{ yr}^{-1}$ (Diehl et al. 2006; Robitaille & Whitney 2010).

Measuring the column densities, metallicities, and ionization conditions in HVCs are key steps in elucidating their importance in Galactic evolution. These parameters are best measured in the UV, where a rich variety of elements and ion stages is accessible through their resonance absorption lines, which are sensitive to column densities well below that detectable in 21-cm emission. For example, Si III $\lambda 1206.5$ is easily detectable with *HST* at column densities $N_{\text{SiIII}} \gtrsim 10^{12} \text{ cm}^{-2}$, corresponding to total hydrogen column densities $N_{\text{H}} \gtrsim (3 \times 10^{16} \text{ cm}^{-2})(Z_{\odot}/Z)$, scaling inversely with metallicity. The high-quality data achievable with COS (signal-to-noise $S/N \gtrsim 30$) provide much better definition of the velocity extent of these HVCs, many of which do not exhibit narrow Gaussian absorption profiles. The ions commonly accessible to the COS G130/G160M gratings include O I, N I, N V, C II, C IV, Si II, Si III, Si IV, S II, Al II, Fe II, Ni II, and P II.

In this paper, we present high-quality, far-UV spectroscopic observations of absorption along four sight lines passing through Complex C. One of the most prominent HVCs, Complex C extends over Galactic longitudes from $\ell \approx 30^{\circ}$ to 150° in the Northern Galactic hemisphere (see maps by Wakker 2001, CSG03, Fox et al. 2004). Multiple sight lines pierce Complex C, with UV-determined metallicities ranging from 10–30% solar (Wakker et al. 1999; CSG03, CSG07). The recent distance estimate of $d = 10 \pm 2.5 \text{ kpc}$ (Wakker et al. 2007; Thom et al. 2008) confirms that it has a substantial mass ($\sim 10^7 M_{\odot}$). As Complex C falls into the Galactic disk over the next 50–100 Myr, it will deliver an average mass inflow of $\sim 0.1 M_{\odot} \text{ yr}^{-1}$, some 5% of the disk replenishment rate for star formation.

Our spectral data were obtained with the moderate-resolution ($R \approx 18,000$) gratings, G130M and G160M, on the Cosmic Origins Spectrograph (COS) on *HST* (Green et al. 2011;

Osterman et al. 2011). The typical COS wavelength coverage is from 1133–1796 Å, although individual spectra extend slightly outside this range: Mrk 817 (1134.5–1796.1 Å), Mrk 876 (1135.4–1795.3 Å), Mrk 290 (1134.1–1796.2 Å), PG 1259+593 (1133.9–1796.1 Å). These UV spectra demonstrate COS capabilities for detecting HVCs along sight lines to background AGN, with several improvements over previous studies. First, the much greater far-UV throughput of the COS gratings provides higher signal-to-noise (S/N) and better photometric accuracy. Second, the low background of the COS detectors allows us to characterize the zero flux levels, important for measurements of column densities of mildly saturated absorption lines. Third, the combination of G130M/G160M gratings offers broad wavelength coverage and access to numerous ion species and resonant lines not covered previously, with either the Goddard High Resolution Spectrograph (GHRS) or *FUSE*. In particular, our COS spectra measure species (Al II, C IV, Si IV) and transitions (O I, Si II, Fe II, P II) not typically measured or reported in GHRS data. Detecting HVCs in multiple ionization stages of the same element such as silicon (Si II, Si III, Si IV) provides diagnostics of the ionization conditions and metallicity of the HVCs, while higher ionization stages (C IV, N V, O VI, Si III, Si IV) are useful in separating the contribution of hot collisionally ionized gas from warm photoionized gas.

In §2 we discuss the observations and data reduction techniques for the COS gratings (G130M and G160M) and 21-cm spectra from the NRAO² Green Bank Telescope (GBT). In §3 we display the data and describe our analysis. In §4 we summarize our observations and their implications for Complex C (metallicity, ionization state, and velocity structure).

2. Observations of Complex C

In this section, we describe the HST/COS ultraviolet spectra of four AGN sight lines (Table 1) passing through Complex C, with absorption typically appearing at LSR velocities $V_{\text{LSR}} \approx -160$ to -90 km s⁻¹. Figure 1 illustrates the locations of our background AGN targets relative to the 21-cm emission from the Leiden-Argentine-Bonn (LAB) survey (Kalberla et al. 2005) with angular resolution $\sim 0.6^\circ$, spectral resolution 1.3 km s⁻¹, and 70–90 mK rms noise in brightness-temperature (T_b). These four sight lines exhibit a wide range in H I column densities from $\log N_{\text{HI}} = 19.39$ to 20.05 (Table 2). Figure 2 shows the combined G130M/G160M ultraviolet spectra from COS, over the wavelength range 1135–1796 Å. New 21-cm spectra taken at the GBT are shown in Figure 3.

²The National Radio Astronomy Observatory is a facility of the National Science Foundation, operated under a cooperative agreement with Associated Universities, Inc.

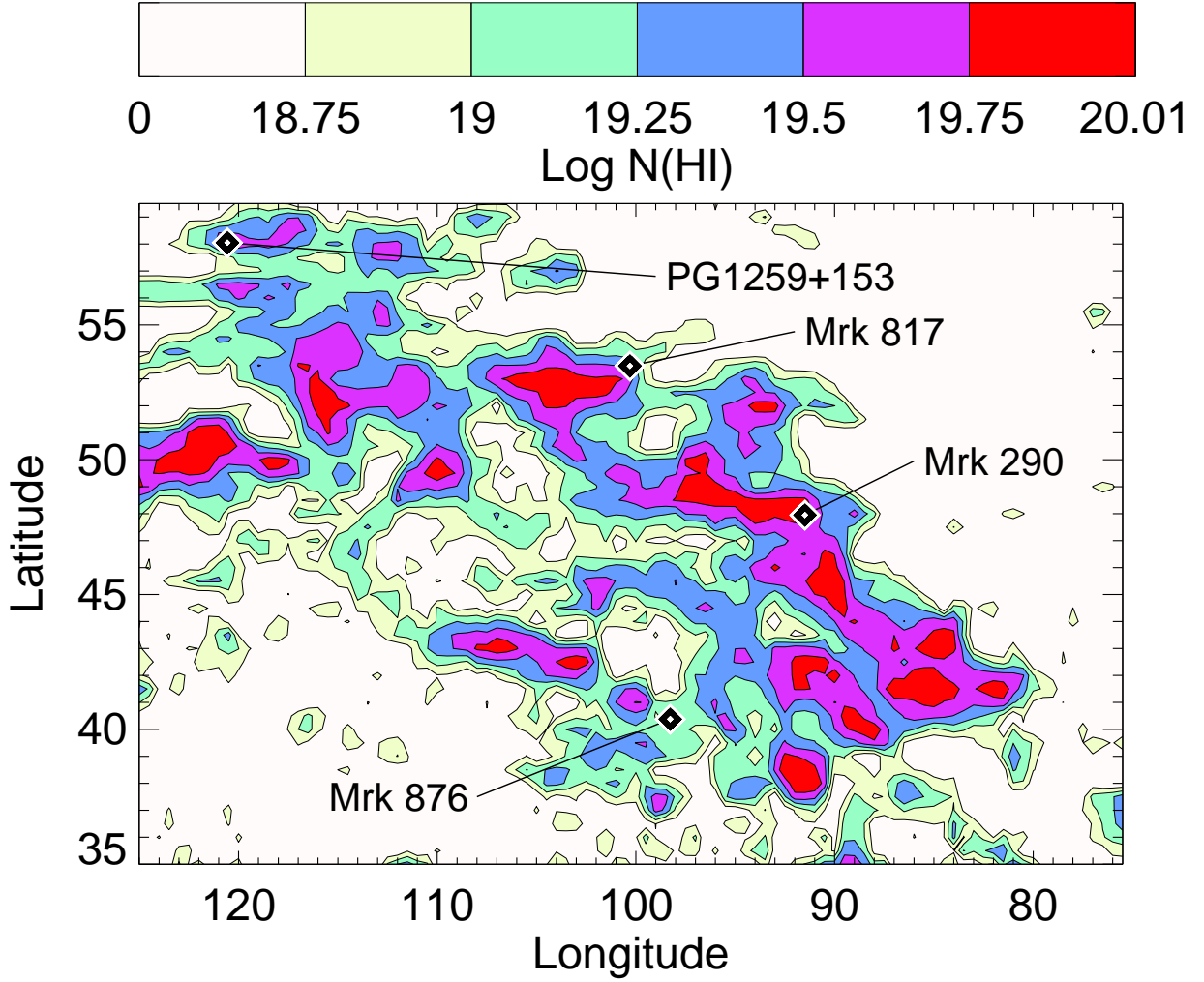


Fig. 1.— Map of our 4 AGN targets overlaid on the contour-map of 21-cm emission from the Leiden-Argentine-Bonn (LAB) survey (Kalberla et al. 2005) with $\sim 0.6^\circ$ angular resolution on a 0.5° grid in ℓ and b . Emission is shown over Galactic coordinates between $\ell = 75 - 125^\circ$ and $b = 35 - 60^\circ$ and over Complex-C velocities between -210 and -95 km s^{-1} . At the 10 kpc distance of Complex C, 1 degree corresponds to 175 pc.

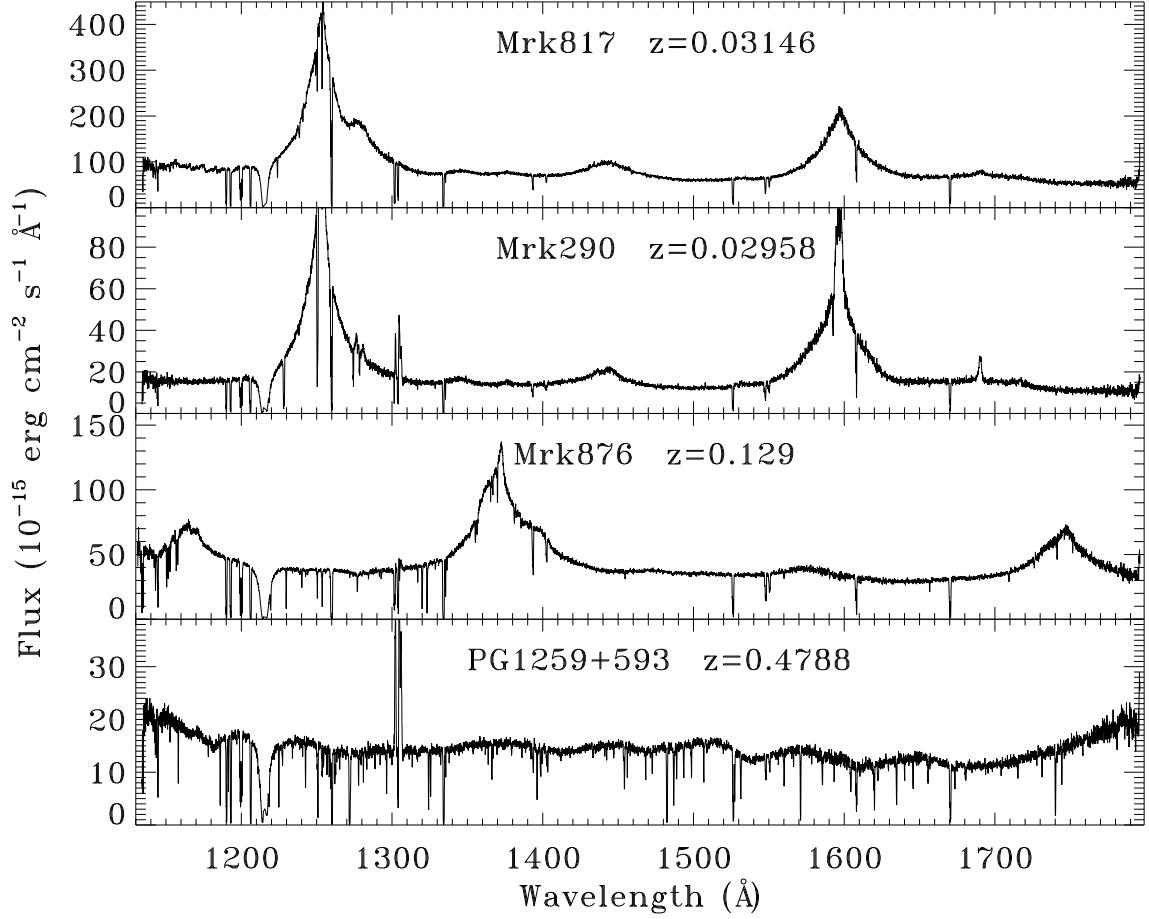


Fig. 2.— Combined G130M/G160M spectra from HST/COS of the four AGN targets behind Complex C over the wavelength range 1135–1796 \AA . Note the prominent broad emission lines, Ly α λ 1216, Si IV/O IV] λ 1400, C IV λ 1549, together with numerous narrow absorption lines from the ISM and IGM. Fluxes are in units of $10^{-15} \text{ erg cm}^{-2} \text{ s}^{-1} \text{ \AA}^{-1}$.

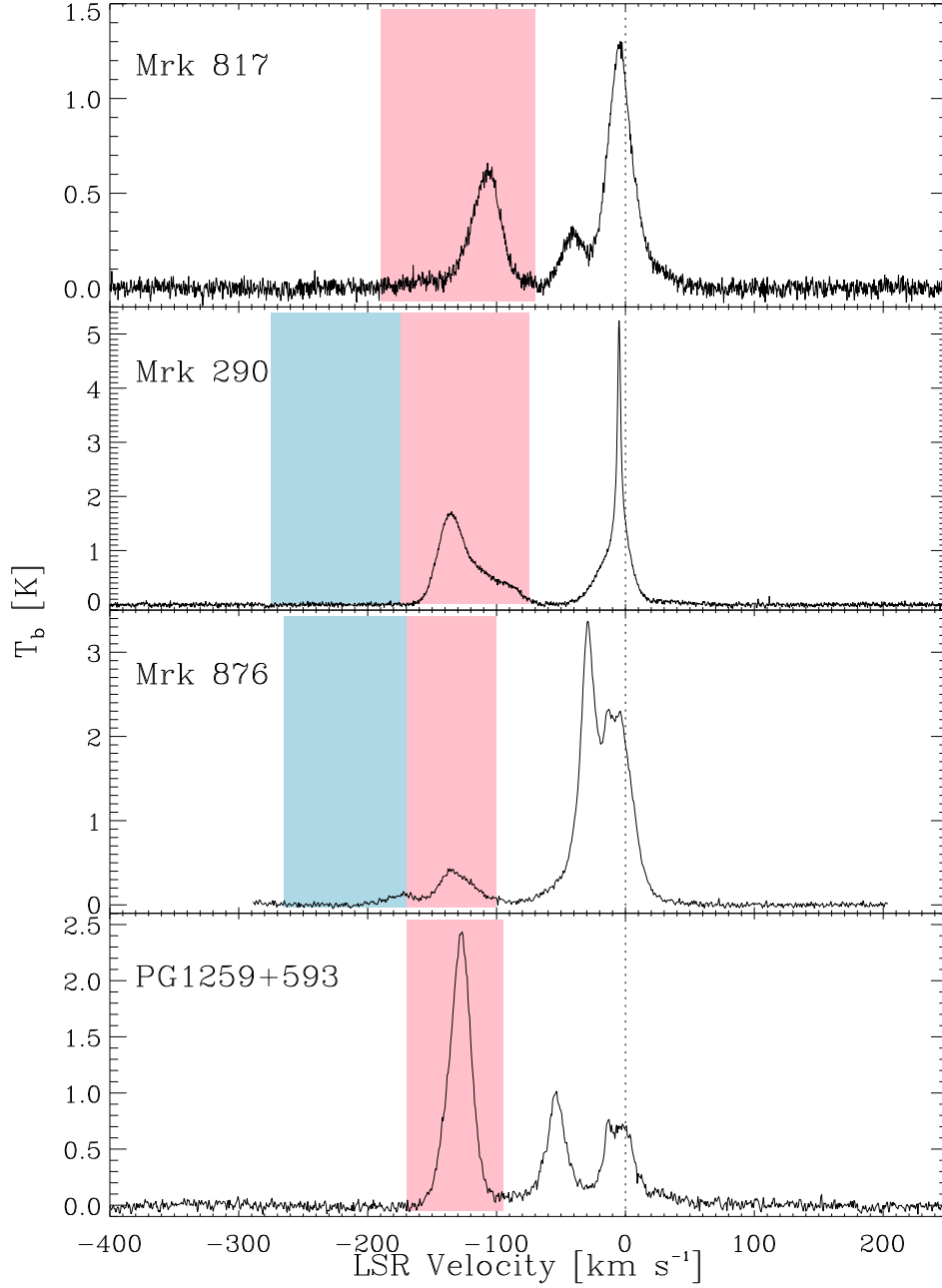


Fig. 3.— Spectra of 21-cm emission toward our four target AGN, taken with the GBT. Velocity ranges in pink wash (Complex C) and blue wash (higher velocity gas) show where we detected high-velocity UV absorption with COS: Mrk 817 (-190 to -70 km s^{-1}); Mrk 290 (-175 to -75 km s^{-1} and -275 to -175 km s^{-1}); Mrk 876 (-170 to -100 km s^{-1} and -265 to -170 km s^{-1}); PG 1259+593 (-170 to -95 km s^{-1}).

2.1. Hubble–COS Observations

Our selected AGN sight lines (Mrk 290, Mrk 817, Mrk 876, PG 1259+593) are the first of many AGN targets, scheduled over three years of COS guaranteed-time observations that probe HVCs in Complexes C, A, M, WD, and WB. These HVCs were observed previously with UV spectrographs aboard the *Hubble Space Telescope* (*HST*) and the *Far Ultraviolet Spectroscopic Explorer* (*FUSE*), including the *FUSE* survey of high-velocity O VI (Sembach et al. 2003) and the *HST*/STIS survey of high-velocity Si III (Shull et al. 2009; CSG09). Previously, Mrk 290 was observed with *FUSE* and *HST*/GHRS (Wakker et al. 1999; Gibson et al. 2001; CSG03, CSG07). Mrk 817 was observed with *HST*/GHRS and *FUSE* (Gibson et al. 2001; CSG03; Fox et al. 2004, 2006). PG 1259+593 was observed with *HST*/STIS and *FUSE* (Richter et al. 2001; CSG03, CSG07; Sembach et al. 2004; Fox et al. 2004, 2006). Mrk 876 was observed with *HST*/GHRS and *FUSE* (Gibson et al. 2001; CSG03, CSG07; Fox et al. 2004; Sembach et al. 2003).

Table 1 lists the relevant COS observational parameters of the current COS program. Our targets were observed in both the G130M (1134–1480 Å) and G160M (1400–1796 Å) medium-resolution gratings ($R \approx 18,000$, $\Delta v \approx 17 \text{ km s}^{-1}$). The NUV-imaging target acquisitions were performed with the MIRRORA/PSA mode; the COS primary science aperture ($\sim 2.5''$ diameter) yields good centering to maximize throughput and resolving power. Mrk817 was observed during two 2009 epochs (August 4 and December 28). The first-epoch observations were part of the Early Release Observations (ERO) program (11505, PI: Noll), and the second epoch of observations were part of a COS Guaranteed Time Observations (GTO) program (11524, PI: Green). The first observations were obtained during the Servicing Mission Orbital Verification (SMOV) period before the instrument reached final focus. However, the pre-focus data are largely indistinguishable from that taken after correct focus had been achieved except in the case of the very narrowest of absorption features ($\Delta\lambda \lesssim 0.1 \text{ Å}$), none of which are analyzed in this work. Another symptom unique to the early SMOV data was the “divot and clod” feature which occurred near the blue end of each detector segment; charge resulting from photons hitting one part of the detector appeared in a different part. The high voltage on the detectors was reduced on 2009, August 4, and the instrumental feature disappeared. For the Mrk817 ERO observations, the divot and clod were carefully fitted with Gaussian profiles and normalized to the flux level in adjacent portions of the spectrum. The observing time was approximately equal at both epochs, but the AGN continuum flux decreased by a factor of 1.4 in the interim. Data from the second epoch were scaled multiplicatively to the flux level of the 2009 August observations. A full discussion of the Mrk 817 data appears in Winter et al. (2011). Targets Mrk 290 and PG 1259+593 were both observed as part of COS/GTO programs 11524 (2009 October 29) and 11541 (2010 April 15) respectively. Mrk 876 was observed (2009 April 8–10)

in our COS/GTO program and as a Guest Observer (GO) target (11686, PI: Arav). The observations were taken within two days of each other.

After retrieval from the STScI, all data were reduced with the COS calibration pipeline, CALCOS³ v2.11f. The analog nature of the COS micro-channel plate makes it susceptible to temperature changes. Electronically injected pulses (stims) at opposite corners of the detector allow for the tracking and correction of any drift (wavelength zero-point) and/or stretch (dispersion solution) of the recorded data location as a function of temperature. Flat-fielding, alignment, and coaddition of the processed COS exposures were carried out using IDL routines developed by the COS GTO team specifically for COS FUV data⁴. The data were corrected for narrow instrumental features arising from shadows from the ion repeller grid wires. We aligned each exposure by cross-correlating strong ISM features and interpolated the aligned exposures onto a common wavelength scale. Wavelength shifts were typically on the order of a resolution element ($\sim 0.07 \text{ \AA}$, 17 km s^{-1}) or less. The coadded flux at each wavelength was taken to be the exposure-weighted mean of flux in each exposure.

To transfer the COS data to the V_{LSR} scale of the 21-cm data, we first aligned the interstellar absorption features in velocity space. Next we chose between 8 and 12 clearly defined HVC absorption features, found the velocity at which their fluxes were minimized, and took the mean. This mean velocity was subtracted from the velocity of the H I 21-cm HVC emission peak, and the resulting difference was used to shift the COS data to align with the 21-cm data. To quantify the quality of the combined data, we identify line-free continuum regions at various wavelengths, smooth the data by the seven-pixel resolution element, and define $(S/N)_{\text{res}} = \text{mean}(\text{flux})/\text{stddev}(\text{flux})$. The S/N varies across the wavelength range, but representative values in G130M and G160M data are shown in Table 1.

Previous observations from *FUSE* and *HST*/GHRS and *HST*/STIS (CSG03, CSG07; Fox et al. 2004, 2006) were reported on all four sight lines (Mrk 290, Mrk 817, Mrk 876, PG 1259). We included *FUSE* data (HVC lines of C III and O VI) and remeasured O VI $\lambda 1031.93$, using the velocity range defined by the HVC absorbers measured by COS. With the higher S/N, these spectra provide better definition of the extent of high-velocity UV absorption. Tables 3–6 provide the equivalent widths, W_{λ} , absorption-line data, and derived column densities. Our error bars include statistical fluctuations in the measurement of equivalent widths and systematic errors arising from variations in the continuum placement

³See the HST Cycle 18 COS Instrument Handbook for more details:
http://www.stsci.edu/hst/cos/documents/handbooks/current/cos_cover.html

⁴See <http://casa.colorado.edu/~danforth/costools.html> for our coaddition and flat-fielding algorithm, which was further described in Danforth et al. (2010).

and HVC velocity range of integration. Our measurements of equivalent widths vary the continuum placement by one standard deviation in continuum flux and adjust the velocity range of HVC absorption by 10 km s^{-1} . These errors are then added in quadrature to produce 1σ confidence limits on our AOD measurements.

The *HST*/COS data on P II $\lambda 1152.82$ and the N I triplet $\lambda 1199.54, 1200.22, 1200.70$ (toward Mrk 817, Mrk 876, PG 1259) are much better determined than the *FUSE* upper limits. Other lines in common include Fe II $\lambda 1143.22, 1144.94$. The complex line profiles of S II and Si II are greatly improved in quality, particularly the S II lines toward Mrk 876 and Mrk 290. We are also able to provide reliable measurements of N I, P II, Al II, and key high ions (C IV, Si IV, N V).

2.2. GBT Observations

The 21 cm H I data used here were all obtained with the Robert C. Byrd Green Bank Telescope (GBT) of the NRAO at an angular resolution of $9'$. The spectrum for Mrk 876 is that published by Wakker, Lockman, & Brown (2011), the spectrum toward PG 1259+593 was obtained from archival GBT data, and new observations were made for Mrk 817 and Mrk 290. In all cases, the data were reduced, calibrated and corrected for stray radiation following the method outlined in Blagrove, Lockman, & Martin (2010) and Boothroyd et al. (2011, in preparation). This technique has been shown to produce 21-cm spectra of HVCs, with errors of a few percent in total N_{HI} limited by noise and residual instrumental baseline effects. We fitted a second-order polynomial to emission-free regions of each spectrum and smoothed the spectra to produce the following velocity resolution and rms noise: Mrk 876 (0.81 km s^{-1} , 19 mK); PG 1259+593 (0.64 km s^{-1} , 30 mK); Mrk 817 (0.32 km s^{-1} , 27 mK); and Mrk 290 (0.32 km s^{-1} , 25 mK).

Table 2 presents Gaussian fits to the 21-cm HVC components, including their velocities, widths, and H I column densities. We calculated H I column densities for the HVCs in the optically thin assumption (see footnote to Table 2), which introduces a negligible error for the weak HVC lines. The free parameters are the line centers (V_{LSR}) of the Gaussians, and their height (brightness temperature T_b) and full-width at half maximum (FWHM in km s^{-1}). We detected H I emission from all HVCs seen in the COS data, except for the most negative velocity component ($V_{\text{LSR}} = -275 \text{ km s}^{-1}$ to -175 km s^{-1}) toward Mrk 290. For this range, we estimate an upper limit from the noise in the 21 cm spectrum integrated over the velocity range of the HVC.

All these directions were observed previously in the 21 cm line by Wakker et al. (2001)

using the Effelsberg radio telescope (9'.7 beam). The GBT data (9'.0 beam) have lower noise by factors of 2 to 4, slightly better angular resolution, and better spectral baselines. The higher GBT signal-to-noise allows us to fit two components to the HVC toward PG 1259+593, whereas Wakker et al. (2001) fitted only one. In general, the two telescopes give similar values of N_{HI} , to within the errors, except for the -136 km s^{-1} component of Mrk 290, where the GBT value is 20% below that from Effelsberg, and the -131 km s^{-1} component of Mrk 876, where the GBT value lies 32% above. In the latter case, the Effelsberg spectrum appears to have been affected by interference. As noted in the captions to Tables 3–6, the total HVC column densities, $\log N_{\text{HI}}$, used in this paper (GBT) are similar to those from Effelsberg (Eff): Mrk 817 (19.50 ± 0.01 from GBT, 19.51 ± 0.01 from Eff); Mrk 290 (20.05 ± 0.01 from GBT, 20.10 ± 0.02 from Eff); Mrk 876 (19.39 ± 0.02 from GBT, 19.30 ± 0.02 from Eff); PG 1259+593 (19.97 ± 0.02 from GBT, 19.95 ± 0.01 from Eff). The primary differences are in the emission-line profiles.

3. Scientific Results and Analysis

3.1. Spectra of HVC Absorption Lines

To illustrate the complexities of identifying an HVC in actual UV absorption-line spectra, it is helpful to show true fluxes vs. wavelength, before deriving equivalent widths from flux-normalized spectra. The UV spectra of AGN are rich in interstellar lines of metal ions, but they often contain low-redshift IGM absorbers. The interstellar absorbers include low-velocity gas near the local standard of rest (LSR), as well as high-velocity and intermediate-velocity gas.

Figures 4–7 present 12-panel plots showing a standard set of HVC absorbers, ranging from low to high ionization state. The velocities of Complex-C absorption are shown in pink wash. Along two sight lines (Mrk 290 and Mrk 876), additional HVCs at higher negative velocity are shown in blue wash. We show selected interstellar spectral features for the four AGN sight lines: absorption lines of eight low-ionization species (C II, N I, O I, S II, Si II, Fe II, Al II, P II) and four more highly ionized species (Si III, Si IV, C IV, N V). We also re-analyzed the O VI data from *FUSE*, using the velocity ranges of HVC ultraviolet absorption, defined by absorption lines of N I, O I, Si II, S II, Fe II, and Al II. In many panels, we show multiple transitions of the same species, including the N I triplet (1199.550, 1200.223, 1200.710 Å), the S II triplet (1250.584, 1253.811, 1259.510 Å), the doublets of C IV (1548.195, 1550.770 Å), Si IV (1393.755, 1402.770 Å), and N V (1238.821, 1242.804 Å), two Si II lines (1190.416, 1193.290 Å), and two lines from the C II ground state (1334.532 Å) and C II* fine-structure state (1335.663 Å). One panel shows lines from O I (1302.168 Å)

and Si II (1304.370 Å), and other panels show lines of Si II (1526.707 Å) and Fe II (1143.226, 1144.938 Å, and 1608.451 Å).

The HVC absorption lines are analyzed to provide absorption equivalent width, W_λ , effective line width (b_{width}), and column density, N . The column densities were derived using the “apparent optical depth” (AOD) method (Sembach & Savage 1992), which yields the column density, $N_a(v)$, in a given velocity interval. We then derive the total column density by integrating $N_a(v)$ over the velocity range of the HVC. A few of the lines (Si III, Al II) are mildly saturated, but we have checked the column densities from the AOD method with the CoGs for these sight lines, determined from the low ions (CSG03) for accuracy. We believe they are reasonable estimates; further discussion is given in Section 3.4.

The COS line spread function (LSF) has broad wings with significant power, as documented on the STScI/COS website in an article (Kriss et al. 2011, COS ISR2011-01) entitled “Improved Medium Resolution Line Spread Function for the COS FUV Spectrum”. Our COS data-reduction software accounts for the LSF when fitting Voigt profiles to absorption lines, but the LSF is not included in the AOD method for deriving column densities, $N_a(v)$, in fixed velocity bins. Thus, some of the increased velocity range could be instrumental in nature, rather than due to the physical nature of the gas itself. However, the differences in velocity and O VI column densities are not large, as we discuss in the notes on individual sight lines (Section 3.5).

Figures 8–11 show “stack plots” of the HVC absorbers, aligned in velocity space using normalized continua. Our previous experience with the COS wavelength scale (Osterman et al. 2011) suggests that differential shifts up to 10 km s^{−1} are possible, relative to the 21 cm emission data. In general, the HVC absorption in the UV metal lines agrees well with the H I emission, with the exception of the Mrk 876 sight line. In that case, we integrate the UV absorption in Complex C over the range $V_{\text{LSR}} = -170$ km s^{−1} to -100 km s^{−1}, whereas the H I emission appears to have a dip at $\langle V_{\text{LSR}} \rangle = -160$ km s^{−1}, separating Complex C from higher-velocity absorption centered at $\langle V_{\text{LSR}} \rangle = -190$ km s^{−1} (see Figures 6 and 10).

From the normalized COS absorption-line data, we derive equivalent widths, line widths, and column densities, which are displayed in Tables 2–5. Details on some of the judgements made in determining column densities are given in Section 3.4. Tables 7–10 compare previous measurements of ion column densities, $\log N(X_i)$, together with our adopted values. We also show the ion ratios referenced to $\log N_{\text{HI}}$ and the corresponding elemental abundances.

3.2. HVC Column Densities and Abundances

Tables 7–10 list the adopted abundances, relative to solar values taken from a recent review (Asplund et al. 2009). On a logarithmic scale where hydrogen is 12.00, these solar values are: C (8.43), N (7.83), O (8.69), S (7.12), Si (7.51), Fe (7.50), Al (6.45), and P (5.41). The previous Complex-C abundance estimates were derived from [O I/H I] and [S II/H I]. The O I measurements should provide an accurate determination of [O/H], owing to the strong resonant charge-exchange coupling of O I and O II with H II and H I. However, in many the sight lines, the O I line ($\lambda 1302.16$) is saturated, and we adopted previous values from weaker lines in the *FUSE* band. Abundances from other ions such as [S II/H I], [Si II/H I], and [Fe II/H I] require ionization corrections to arrive at the true metallicities of these elements. There is no guarantee that all elements have the same metallicity, owing to the chemical history of the HVC or possible dust depletion of refractory elements (Si, Al, Fe). As shown in our previous work (see Fig. 16 of CSG03), these corrections are typically expressed as the logarithmic difference between the ion abundance and elemental metallicity. For example, the difference [S II/H I]–[S/H] ranges from 0.1–0.6 for H I column densities $\log N_{\text{HI}} = 19.4$ – 20.1 and HVC physical densities $n_H = 0.01$ – 0.1 cm^{-3} . The HVC metallicities are usually found from [O I/H I], which requires no ionization correction (CSG03, CSG07), and from [S II/H I], reduced by a factor that depends on the H I column density.

Our four AGN sight lines fall into two distinct groups: one with low column density (Mrk 876 and Mrk 817 have $\log N_{\text{HI}} \approx 19.4 - 19.5$) and one with high column density (Mrk 290 and PG 1259+593 have $\log N_{\text{HI}} \approx 20.0 - 20.1$). The ionization corrections to the metal ions (CSG03) depend on the “photoionization parameter”, the ratio of ionizing radiation field to gas density n_H . As seen in Figure 1, the HVC clumps have characteristic angular sizes of $1^\circ - 2^\circ$, perhaps poorly characterized owing to the 0.6° beam and 0.5° sampling grid of the LAB survey. At the 10 kpc distance of Complex C, one degree corresponds to 175 pc. If the H I absorbers have a comparable depth and angular extent, the observed H I column densities correspond to physical densities $n_H \approx 0.05 \text{ cm}^{-3}$ (Mrk 876 and Mrk 817) and $n_H \approx 0.2 \text{ cm}^{-3}$ (Mrk 290 and PG 1259). From our previous photoionization modeling and observed H I column densities, we adopt the following corrections. For Mrk 290 and PG 1259, the corrections are minor: [S II/H I] and [Si II/H I] are reduced by 0.04 (dex) and [Fe II/H I] is reduced by 0.02 (dex). For Mrk 876, we reduce [S II/H I] by 0.32, [Si II/H I] by 0.27, and [Fe II/H I] by 0.14. For Mrk 817, we reduce [S II/H I] by 0.27, [Si II/H I] by 0.21, and [Fe II/H I] by 0.11. We have not made ionization corrections for O I N I, Al II, or P II. The ionization corrections noted above for S II, Si II, and Fe II have been applied and included in the final column in Tables 7–10.

3.3. Inferred Column Densities of Photoionized and Hot Gas

The Si III column density can be used as a proxy for ionized gas to infer the column density, $N(\text{H II})$, of ionized hydrogen that is kinematically associated with the observed H I. As discussed by Shull et al. (2009), the Si III ion likely includes contributions from both photoionized and collisionally ionized gas (only 16.34 eV needed to produce Si III). We adopt an ionization fraction $f_{\text{SiIII}} = 0.7 \pm 0.2$ characteristic of multiphase conditions. Following the methodology of our Si III survey with *HST*/STIS (Shull et al. 2009), we assume a metallicity $Z_{\text{Si}} \approx 0.1$ relative to the solar abundance, $(\text{Si}/\text{H})_{\odot} = 3.24 \times 10^{-5}$, to find:

$$N_{\text{HII}} = (4.4 \times 10^5) N_{\text{SiIII}} \left[\frac{Z_{\text{Si}}}{0.1} \right]^{-1} \left[\frac{f_{\text{SiIII}}}{0.7} \right]^{-1}. \quad (1)$$

For the current four sight lines, we infer ionized column densities, $\log N(\text{H II}) = 18.79$ (Mrk 290), 19.24 (PG 1259+593), 19.38 (Mrk 817), and 19.56 (Mrk 876). Comparing to the observed H I, these correspond to ionization fractions, $N(\text{H II})/N(\text{H I})$, ranging from low values of 6–10% in the high-column HVCs toward Mrk 290 ($\log N_{\text{HI}} = 20.05$) and PG 1259+593 ($\log N_{\text{HI}} = 19.97$) to much larger values of 80% and 150% toward Mrk 817 ($\log N_{\text{HI}} = 19.50$) and Mrk 876 ($\log N_{\text{HI}} = 19.39$). Interestingly, the highest ionization fractions occur in the HVCs with the lowest H I column densities. This suggests that the *total* hydrogen column density distribution is smoother than indicated by the 21-cm emission maps.

Using arguments similar to the Si III case, we can use the observed column densities of high ions (e.g., C IV and O VI) to infer the column densities of hot, collisionally ionized gas. The COS data on high ions (N V, C IV, O VI, Si IV, Si III) are new or improved over earlier measurements. Our re-measurements of O VI HVC absorption are compared in Section 3.4 to previous *FUSE* studies (Sembach et al. 2003; Fox et al. 2004; CSG07). In many cases, the COS data have higher S/N, which we use to define the velocity range of HVC absorption. We remeasured O VI column densities using these ranges (see captions to Figures 4–7). The small differences with previous values (Sembach et al. 2003; Fox et al. 2004) are generally within the stated error bars. We adopt metallicities Z_{C} and Z_{O} of 10% solar and assume hot-gas ionization fractions $f_{\text{CIV}} = 0.3$ and $f_{\text{OVI}} = 0.2$. The observed C IV and O VI column densities toward three sight lines (Mrk 817, Mrk 290, Mrk 876) yield consistent “hot gas” column densities $\log N(\text{H II}) = 18.7 - 18.8$, with C IV/O VI abundance ratios consistent, at $N(\text{C IV})/N(\text{O VI}) = 0.4 - 0.5$. The fourth sight line (PG 1259+593) has the lowest C IV and O VI column densities, resulting in a lower inferred $\log N(\text{H II}) = 18.2 - 18.3$ and a slightly lower ratio, $N(\text{C IV})/N(\text{O VI}) = 0.3$.

The ionization ratios, C IV/O VI, N V/O VI, Si IV/O VI, can be compared with observations of highly ionized HVCs (Fox et al. 2004, 2005, 2006; CSG05; CSG07; Indebetouw

& Shull 2004b) and with models of various ionization processes (see Figure 1 of Indebetouw & Shull 2004a). In ratio plots of C IV/O VI and N V/O VI, the regions occupied by HVCs along our four sight lines are consistent with hot gas in conductive or radiatively cooling interfaces. The observed ratios are *not* consistent with collisional ionization equilibrium (CIE) or turbulent mixing layers (TML). For relative solar abundances (O: C: N = 1.00: 0.55: 0.14), the CIE models produce much higher N V/C IV ratios than observed; the obvious explanation is the lower nitrogen abundance observed in neutral HVC gas. Models of TMLs exhibit a wide range of predictions, owing to the assumptions and parameterizations that go into calculating the ionization and cooling. Early TML models (Slavin, Shull, & Begelman 1993; Indebetouw & Shull 2004) assumed mixing to an intermediate temperature, $\bar{T} \approx 10^5$ K and relaxed to ionization equilibrium (Slavin, Shull, & Begelman 1993; Indebetouw & Shull 2004a). Those models produce much higher C IV/O VI ratios than observed. More recent TML models (Kwak & Shelton 2010) that incorporate non-equilibrium ionization find regions with warm, radiatively cooled C IV, mixed with hotter gas, out of ionization equilibrium. These models find 2–4 times higher column densities in N V, C IV, and O VI abundances than predicted in CIE. However, their typical TML ratios are: C IV/O VI = 1.5 (range 0.8–2.4) and N V/O VI (range 0.14–0.32), both higher than the COS-observations, which have more O VI than predicted by the models. Models of non-equilibrium ionization (Gnat & Sternberg 2007) with time-dependent cooling ($Z \approx 0.1Z_\odot$) find fair agreement with the COS-observed ionization ratios.

We observe a range of ratios, Si IV/C IV \approx 0.15–0.36, along the four sight lines, typical of the previous studies (Fox et al. 2004, 2005; CSG05; CSG07). For relative solar abundances, $(\text{Si}/\text{C})_\odot = 0.11$, photoionization models of HVCs find abundance ratios, $N(\text{Si IV})/N(\text{C IV}) > 1$, for values of photoionization parameter, $\log U = -3.0 \pm 0.2$, needed to explain the low ions and fit the ratios Si IV/Si III/Si II (Shull et al. 2009). These same models also under-predict the total column densities of high ions (C IV, Si IV, N V, O VI). Similarly, photoionization models with the observed range, $N(\text{Si IV})/N(\text{C IV}) = 0.1\text{--}0.3$, predict $N(\text{Si IV})/N(\text{Si II}) \approx 1$, much higher than observed. Therefore, it is likely that some C IV and Si IV comes from hot gas. The kinematic association of low and high ions in these HVCs requires a mixture of denser cloud cores of H I with extended warm photoionized gas and sheaths of much hotter gas, perhaps produced by bow shocks and turbulent or conductive interfaces between the HVC core and hot halo gas. However, detailed comparisons of observations and models are often complicated by the assumptions of *relative* solar abundances.

3.4. Toy Model for HVC Clouds in the Galactic Halo

One of the reasons for renewed interest in Galactic HVCs is the possibility that the Local Group might contain considerable mass in virialized halos and a hot circumgalactic medium. Spitzer (1956) first suggested the existence of low-density coronal gas with $T = 10^6$ K and $n_e = 5 \times 10^{-4} \text{ cm}^{-3}$, extending 8 kpc above the Galactic plane and providing pressure confinement of observed high latitude clouds. Kahn & Woltjer (1959) noted inconsistencies in galactic stellar masses and Local Group dynamics (before the inference of dark matter) and suggested the existence of a substantial reservoir of low-density halo gas, with $T = 5 \times 10^6$ K and $n_e = 1 \times 10^{-4} \text{ cm}^{-3}$. Direct probes of hot, low-density gas are difficult, owing to the n^2 dependence of its X-ray emission and the contamination of most signals by foreground electrons in the kpc-scale “Reynolds layer” (Reynolds 1991). Indirect probes of the halo density yield limits ($n_e < 10^{-4} \text{ cm}^{-3}$) from the effects of drag on orbits of the Magellanic Stream (Moore & Davis 1994). Similar limits ($n_e < 3 \times 10^{-5} \text{ cm}^{-3}$) follow from ram-pressure stripping of Local Group dwarf galaxies (Blitz & Robishaw 2000). More recently, Heitsch & Putman (2009) used numerical simulations to suggest that infalling HVCs with H I masses less than $10^{4.5} M_\odot$ may become fully ionized by Kelvin-Helmholtz instabilities within 10^8 yr (~ 10 kpc for typical HVC velocities of 100 km s^{-1}). All of these estimates depend critically on the assumed halo gas density and on dynamical interactions at the boundaries between the HVCs and the hot, low-density medium that confines them.

As a toy model for HVC cloud confinement, we consider spherical clouds with radius R , mass M , constant gas density ρ , and mean atomic mass $\mu = \rho/n_H = 1.23m_H$ (helium 25% by mass) in virial equilibrium confined by external pressure, P_0 . For clumps of angular radius θ_{deg} (in degrees), we adopt $R = (175 \text{ pc})\theta_{\text{deg}}$ at 10 kpc distance, $n_H = (0.1 \text{ cm}^{-3})n_{0.1}$, and temperature $T = (100 \text{ K})T_{100}$. The virial theorem with confinement (Spitzer 1978) requires that

$$4\pi R^3 P_0 = \frac{3MkT}{\mu} - \frac{3GM^2}{5R}. \quad (2)$$

The confining pressure could arise from hot Galactic halo gas, which we scale to nominal values $n_{\text{halo}} = (10^{-5} \text{ cm}^{-3})n_{-5}$ and $T_{\text{halo}} = (10^6 \text{ K})T_6$. Alternately, the HVCs could be confined by ram pressure, $P_{\text{ram}} = \rho_{\text{halo}}V_{\text{HVC}}^2$, as they fall through the halo. For the assumed halo parameters, the total thermal pressure of fully ionized gas with $n_{\text{He}}/n_{\text{H}} = 0.0823$ is $P/k \approx 2.25n_H T = (22.5 \text{ cm}^{-3} \text{ K})n_{-5} T_6$. This pressure is consistent with inferences from various highly ionized HVCs (Sembach et al. 1999; CSG05), although such estimates are uncertain owing to assumptions in the ionization modeling. The halo density probably lies in the range $n_e = (1 - 10) \times 10^{-5} \text{ cm}^{-3}$, with considerable variation over vertical distances 5–50 kpc above the Galactic plane.

In our model, the HVC clump masses in Complex C are $M = (6.8 \times 10^4 M_\odot) n_{0.1} \theta_{\text{deg}}^3$, and the terms in the virial equation are all of comparable size,

$$(3MkT/\mu) = (2.7 \times 10^{48} \text{ erg}) n_{0.1} T_{100} \theta_{\text{deg}}^3 \quad (3)$$

$$(3GM^2/5R) = (1.4 \times 10^{48} \text{ erg}) n_{0.1}^2 \theta_{\text{deg}}^5 \quad (4)$$

$$4\pi R^3 P_0 = (4.0 \times 10^{48} \text{ erg}) [n_{\text{halo}}/10^{-5} \text{ cm}^{-3}] \theta_{\text{deg}}^3. \quad (5)$$

The thermal pressure of the halo, $P_{\text{halo}} \approx 1.6 \times 10^{-15} \text{ erg cm}^{-3}$, is comparable to the ram pressure on the HVCs. This not surprising, as these infalling clouds have low Mach numbers with respect to the hot gas. The HVC clumps may not be self-gravitating (no H_2 or stars have been detected). However, their observed properties place them near virial equilibrium (with $T \leq 10^3 \text{ K}$), and there may be no need to invoke dark matter for their confinement.

As the HVCs encounter the higher densities in the stratified lower halo, their outer portions may be torn apart and dissipated by interface instabilities. This would feed the Galactic halo rather than replenishing the reservoir of star formation in the disk. Portions of Complex C do appear to be clumping up, although the individual clump masses ($\theta_{\text{deg}} \geq 1$) are likely above the $10^{4.5} M_\odot$ threshold for survival (Heitsch & Putman 2009).

3.5. Notes on Individual Sight Lines

In this section, we compare the COS equivalent widths of several lines, previously measured by GHRS and STIS spectrographs (CSG03, CSG07; Richter et al. 2001). The derived column densities of various ions are compared in Tables 7–10. For some of the high ions (C IV, Si IV, Si III, N V) our COS measurements are the only published data. Previous measurements of high-velocity Si III toward Mrk 876 and PG 1259+593 were discussed in the *HST* surveys by Shull et al. (2009) and Collins et al. (2009).

(1) Mrk 817. The three unsaturated S II lines at 1250, 1253, and 1259 Å should have equivalent widths in the ratio 1:2:3 based on their relative oscillator strengths. The weakest line ($\lambda 1250.6$) was measured at $W_\lambda = 27 \pm 8 \text{ mÅ}$ (COS) vs. $16 \pm 3 \text{ mÅ}$ (GHRS). The stronger line ($\lambda 1253.8$) was $19 \pm 5 \text{ mÅ}$ (COS) vs. $28 \pm 3 \text{ mÅ}$ (GHRS). The strongest line ($\lambda 1259.5$) with $42 \pm 7 \text{ mÅ}$ (COS) was not reported with GHRS. We base our S II column density, $\log N = 14.29 \pm 0.08$, on the $\lambda 1259$ measurement. For other lines we used Si IV $\lambda 1394$, N V $\lambda 1238$, Si II $\lambda 1304$ (consistent with $\lambda 1526$), and Fe II $\lambda 1608$ (consistent with $\lambda 1145$). We find good agreement between both lines in the doublets of C IV ($\lambda \lambda 1548, 1551$), N V ($\lambda \lambda 1238, 1242$), and Si IV ($\lambda \lambda 1394, 1402$). Fox et al. (2004) suggested that there may be no detectable high-velocity N V toward Mrk 817 because of intergalactic Ly α absorbers at $z = 0.0189$ and $z = 0.0194$. However, we believe to have detected N V with $\log N =$

$13.16^{+0.12}_{-0.15}$ at the -109 km s^{-1} velocity of Complex C. As seen in Figure 8, the $\text{Ly}\alpha$ absorber at $z = 0.0184$ would appear at -42 km s^{-1} in the N V rest frame, fairly well separated from the HVC. The ratios of N V to other high ions (C IV, Si IV, O VI) are typical of other sight lines. We use the weaker N I $\lambda 1199.5$ line, since the other lines (1200.2 \AA and 1200.7 \AA) are blended with $V_{\text{LSR}} = 0$ absorption. Both Al II $\lambda 1670.78$ and Si III $\lambda 1206.50$ are mildly saturated, at equivalent widths of $\sim 400 \text{ m\AA}$ and $\sim 350 \text{ m\AA}$, respectively. Our inferred column densities from AOD integration of $N_a(v)$ accurately reflect this saturation, for line broadening of $20\text{--}30 \text{ km s}^{-1}$, somewhat higher than the doppler parameter $b = 11 \text{ km s}^{-1}$ inferred from O I and other low ions (CGS03). Re-measuring the O VI column density, we find $\log N = 14.05^{+0.16}_{-0.09}$ compared to $13.97^{+0.10}_{-0.13}$ from Fox et al. (2004) and 13.88 ± 0.20 (Sembach et al. 2003). The small differences in O VI column densities arise from the velocity range adopted for the HVC absorption. From the extent of UV absorption (S II, Si II, Fe II, Al II) in Figure 8, we integrate between $V_{\text{LSR}} = -190$ and -70 km s^{-1} , whereas Fox et al. (2004) used the interval from -160 to -80 km s^{-1} .

(2) Mrk 290. The S II data from COS are superior to that from GHRS or STIS (CSG03, CSG07). The HVC components of $\lambda 1250.57$ and $\lambda 1253.80$ lie in the blue and red wings, respectively, of the broad $\text{Ly}\alpha$ emission line of the AGN (see Fig. 5). To arrive at the column density, $\log N = 14.43 \pm 0.08$, we use the $\lambda 1259.51$ line. For Si II, both lines ($\lambda 1304$ and $\lambda 1526$) are saturated, yielding a lower limit on column density. We adopt the CoG value, $\log N = 14.9 \pm 0.15$, from CSG07. The column density from the mildly saturated Fe II $\lambda 1608$ is consistent with $\lambda 1145$. We see agreement between both lines in the doublets of C IV ($\lambda\lambda 1548, 1551$), N V ($\lambda\lambda 1238, 1242$), and Si IV ($\lambda\lambda 1394, 1402$). We use the weaker line N I $\lambda 1199.5$ line, since the other lines (1200.2 \AA and 1200.7 \AA) are blended with $V_{\text{LSR}} = 0$ absorption. Both Al II $\lambda 1670.78$ and Si III $\lambda 1206.50$ are mildly saturated, at equivalent widths of $\sim 340 \text{ m\AA}$ and $\sim 345 \text{ m\AA}$, respectively. Our inferred column densities from AOD integration of $N_a(v)$ accurately reflect this saturation, for line broadening of $20\text{--}30 \text{ km s}^{-1}$, somewhat higher than the doppler parameter $b = 16 \text{ km s}^{-1}$ inferred from O I and low ions (CGS07). We re-measured the O VI column density, finding reasonable agreement, $\log N = 14.10^{+0.15}_{-0.14}$ (between -175 and -75 km s^{-1}) compared to 14.23 ± 0.04 (CSG07 integrated between -165 and -75 km s^{-1}) and 14.20 ± 0.16 (Sembach et al. 2003).

(3) Mrk 876. The S II data from COS are superior to that from STIS (CSG07), which only gave an upper limit, $\log N < 14.34$. With COS, the HVC components of $\lambda 1259.51$ and $\lambda 1253.80$ yield essentially the same column density, $\log N = 14.25^{+0.13}_{-0.14}$. For Si II, both lines ($\lambda 1304$ and $\lambda 1526$) are mildly saturated, but yield a consistent column density, $\log N = 14.41^{+0.16}_{-0.09}$. The column density from Fe II $\lambda 1608$, $\log N = 14.26^{+0.17}_{-0.10}$, is consistent with that from $\lambda 1145$. We find agreement between both lines in the doublets of C IV ($\lambda\lambda 1548, 1551$), N V ($\lambda\lambda 1238, 1242$), and Si IV ($\lambda\lambda 1394, 1402$). We use the weaker N I

$\lambda 1199.5$ line, since the other lines (1200.2 \AA and 1200.7 \AA are blended with $V_{\text{LSR}} = 0$ absorption. Both Al II $\lambda 1670.78$ and Si III $\lambda 1206.50$ are mildly saturated, at equivalent widths of $\sim 280 \text{ m\AA}$ and $\sim 270 \text{ m\AA}$, respectively. Our inferred column densities from AOD integration of $N_a(v)$ accurately reflect this saturation, for line broadening of 20 km s^{-1} , somewhat higher than the doppler parameter $b = 16 \text{ km s}^{-1}$ inferred from O I and low ions (CGS03). Our previous HVC survey of Si III (Shull et al. 2009) measured $\log N \geq 13.92$ for this absorber, slightly higher than the value, $13.72^{+0.24}_{-0.14}$ measured here. We re-measured the O VI column density, finding moderate differences, but within stated errors, $\log N = 13.99^{+0.36}_{-0.14}$ compared to 14.20 ± 0.02 (CSG07), 14.05 ± 0.17 (Sembach et al. 2003), and $14.12^{+0.11}_{-0.13}$ (Fox et al. 2004). From the observed extent of the UV absorption (S II, Si II, Fe II), we integrate O VI between $V_{\text{LSR}} = -170$ and -100 km s^{-1} , whereas Fox et al. (2004) used the interval from -220 to -100 km s^{-1} , and CSG07 used -210 to -75 km s^{-1} .

(4) PG 1259+593. The S II data from COS are superior to that from GHRS (CSG03) and agree well with those from STIS (Sembach et al. 2004; Richter et al. 2001). Our column density, $\log N = 14.35^{+0.15}_{-0.10}$ agrees with previous measurements. For Si II, both lines ($\lambda 1304$ and $\lambda 1526$) are mildly saturated and yield a consistent column density. The column density from Fe II $\lambda 1608$ is consistent with $\lambda 1145$. We find agreement between both lines in the doublets of C IV ($\lambda 1548, 1551$), N V ($\lambda 1238, 1242$), and Si IV ($\lambda 1394, 1402$). Neither line in the N V doublet ($\lambda 1238, 1242$) is seen, to a limit $\log N < 12.99$ (3σ). We use the weaker N I $\lambda 1199.5$ line, since the other lines at 1200.2 \AA and 1200.7 \AA are blended with $V_{\text{LSR}} = 0$ absorption. Both Al II $\lambda 1670.78$ and Si III $\lambda 1206.50$ are mildly saturated, at equivalent widths of $\sim 215 \text{ m\AA}$ and $\sim 190 \text{ m\AA}$, respectively. Our inferred column densities from AOD integration of $N_a(v)$ accurately reflect this saturation, for line broadening of $20\text{--}30 \text{ km s}^{-1}$, somewhat higher than the doppler parameter $b = 10 \text{ km s}^{-1}$ inferred from O I and low ions (CGS03). Our previous HVC survey of Si III (Shull et al. 2009) measured $\log N \geq 13.60$ for this absorber, somewhat higher than the value, $\log N = 13.30^{+0.24}_{-0.16}$ measured here. We re-measured the O VI column density of this HVC, finding fair agreement, $\log N = 13.58^{+0.18}_{-0.12}$ compared to 13.71 ± 0.09 (Fox et al. 2004) and 13.72 ± 0.17 (Sembach et al. 2003). We integrate between $V_{\text{LSR}} = -170$ and -95 km s^{-1} , while Fox et al. (2004) used the interval from -160 to -80 km s^{-1} . For the O I column density in Complex C, we adopt the careful measurement, $\log N_{\text{OI}} = 15.85 \pm 0.15$ from Sembach et al. (2004), who fitted components as part of their study to find a deuterium ratio, $\text{D}/\text{H} = (2.2 \pm 0.7) \times 10^{-5}$ in this HVC.

4. Conclusions and Implications

The high throughput and low background of the Cosmic Origins Spectrograph allow us to observe Complex HVCs with high S/N and improved velocity accuracy. A summary of the major issues and new observational results follows:

- Comparison of COS/G130M and G160M data with previous HST and FUSE data shows a more complete array of transitions and elements, with higher S/N and a better defined velocity range of UV absorption.
- In general, the COS-derived column densities and abundances agree with previous UV spectroscopic studies by GHRS, STIS, and FUSE. The Complex C metallicity inferred from O I and S II lies between 10–30% of solar values. The better-defined velocity range of UV absorption affects some of the high-ion column densities such as O VI.
- Using Si III as a proxy for H II, we find a substantial amount of ionized gas kinematically associated with the H I 21-cm emission, ranging from $N(\text{H II})/N(\text{H I}) \approx 0.1$ (Mrk 290, PG 1259+593) to 0.8–1.5 (Mrk 817, Mrk 876). The HVCs are expected to have extended ionized atmospheres owing to photoionization, and possibly from interactions with the halo.
- Individual clumps of Complex C appear to be near virial equilibrium with pressure confinement. Their masses ($\geq 10^5 M_\odot$) are probably above the threshold for survival against dissipation by interface instabilities.
- High ionization states (C IV, N V, Si IV, O VI) are seen in all four sight lines, with column densities ranging over factors of 3–5 and ratios consistent with multi-phase ionization processes: $N(\text{Si IV})/N(\text{O VI}) \approx 0.05\text{--}0.11$, $N(\text{C IV})/N(\text{O VI}) \approx 0.3\text{--}0.5$, $N(\text{N V})/N(\text{O VI}) \approx 0.07\text{--}0.13$, and $N(\text{Si IV})/N(\text{Si III}) \approx 0.1\text{--}0.2$. The observed ratios $\text{Si IV}/\text{C IV} \approx 0.15\text{--}0.36$ are inconsistent with photoionization models for the low ions.
- Models of high-ion production and C IV, N V, O VI line ratios in Galactic halo gas (Indebetouw & Shull 2004a,b; Gnat & Sternberg 2007) suggest radiative cooling and conductive heating. They are inconsistent with collisional ionization equilibrium, which produces more N V and less O VI than observed: $N(\text{N V})/N(\text{O VI}) \approx 0.3$ and $N(\text{C IV})/N(\text{O VI}) \approx 0.1$. The low N V probably reflects the nitrogen underabundance observed in the neutral components of many HVCs.

As noted in the Introduction, Complex C is a large ($M \sim 10^7 M_\odot$) HVC with substantial amounts of neutral and ionized gas, falling toward the Galactic plane with an average mass

flow of $0.1 M_{\odot} \text{ yr}^{-1}$ of low-metallicity gas (10–30% solar). Over the entire Galactic halo, as probed by Si III (Shull et al. 2009), HVCs may provide sufficient gaseous infall, $\sim 1 M_{\odot} \text{ yr}^{-1}$ to help replenish some of the $2\text{--}4 M_{\odot} \text{ yr}^{-1}$ of star formation in the disk. Future HVC studies with COS will include sight lines passing through Complex M (Danly et al. 1993; Yao et al. 2011), Complex A (van Woerden et al. 1999), and the Smith Cloud (Lockman et al. 2008). With more accurate metal-ion abundances and ionization corrections, we may soon be able to assess the relative abundance ratios of different elements (S, Si, O, Fe, N, and perhaps P and Al) seeking to find non-solar ratios indicative of chemical history. Nitrogen is underabundant relative to C and S, which suggests that Complex C gas is chemically young.

The abundances of refractory elements (Si, Al, Fe) relative to undepleted S could limit the amount of dust, which is expected to be small, given the lack of clear evidence for infrared emission from Complex C. Typical values for these four sight lines are $(\text{S}/\text{Fe}) \approx 1.0\text{--}1.7$, $(\text{Si}/\text{Fe}) \approx 1.2\text{--}1.7$, and $(\text{Al}/\text{Fe}) \approx 0.06\text{--}0.10$. Because this range is within the uncertainty of the measurements, it is difficult to draw any firm conclusions. The $[\alpha/\text{Fe}]$ ratios are interpreted as the ratio of massive-star nucleosynthesis (and core-collapse SNe) to nucleosynthesis from older stars (and Type Ia SNe, which produce more Fe).

It is our pleasure to acknowledge the thousands of people who made HST Servicing Mission 4 a huge success. We thank Brian Keeney, Stéphane Béland, and the rest of the COS/GTO team for their work on the calibration and verification of the early COS data. We thank Andrew Fox for helpful discussions of his previous studies of the high ions toward Complex C and Mark Giroux for insights on photoionization modeling of HVCs. We also appreciate comments from the referee, Kenneth Sembach, on physical conditions in HVCs and details of the COS data analysis. This work was supported by NASA grants NNX08AC146 and NAS5-98043 and the Astrophysical Theory Program (NNX07-AG77G from NASA and AST07-07474 from NSF) at the University of Colorado at Boulder.

REFERENCES

- Asplund, M., Grevesse, N., Sauval, A. J., & Scott, P. 2009, *ARA&A*, 47, 481
- Blagrove, K., Lockman, F. J., & Martin, P. G. 2011, to appear in *The Dynamic ISM: A celebration of the Canadian Galactic Plane Survey*, ASP Conference Series
- Blitz, L., & Robishaw, T. 2000, *ApJ*, 541, 675
- Collins, J. A., Shull, J. M., & Giroux, M. L. 2003, *ApJ*, 585, 336
- Collins, J. A., Shull, J. M., & Giroux, M. L. 2004, *ApJ*, 605, 216
- Collins, J. A., Shull, J. M., & Giroux, M. L. 2005, *ApJ*, 623, 196
- Collins, J. A., Shull, J. M., & Giroux, M. L. 2007, *ApJ*, 657, 271
- Collins, J. A., Shull, J. M., & Giroux, M. L. 2009, *ApJ*, 705, 962
- Danforth, C. W., & Shull, J. M. 2008, *ApJ*, 679, 194
- Danforth, C. W., Keeney, B. A., Stocke, J. T., Shull, J. M., & Yao, Y. 2010, *ApJ*, 720, 976
- Danly, L., Albert, E., & Kuntz, K. D. 1993, *ApJ*, 416, L29
- Dekel, A., & Birnboim, Y. 2006, *MNRAS*, 368, 2
- Diehl, R., et al. 2006, *Nature*, 439, 45
- Erb, D. K., Shapley, A. E., Pettini, M., et al. 2006, *ApJ*, 644, 813
- Fox, A. J., Savage, B. D., Wakker, B.P., et al. 2004, *ApJ*, 602, 738
- Fox, A. J., Wakker, B. P., Savage, B. D., et al. 2005, *ApJ*, 630, 332
- Fox, A. J., Savage, B. D., & Wakker, B. P. 2006, *ApJS*, 165, 229
- Gibson, B. K., Giroux, M. L., Penton, S. V., et al. 2000, *AJ*, 120, 1830
- Gibson, B. K., Giroux, M. L., Penton, S. V., et al. 2001, *AJ*, 122, 3280
- Gilmore, G. 2001, in *Galaxy Disks & Disk Galaxies*, ASP Conf. Ser., 230, 3
- Gnat, O., & Sternberg, A. 2007, *ApJS*, 168, 213
- Green, J., Froning, C. S., et al. 2011, *ApJ*, submitted
- Heitsch, F., & Putman, M. 2009, *ApJ*, 698, 1485
- Indebetouw, R., & Shull, J. M. 2004a, *ApJ*, 605, 215
- Indebetouw, R., & Shull, J. M. 2004b, *ApJ*, 607, 309
- Kahn, F. D., & Woltjer, L. 1959, *ApJ*, 130, 705
- Kalberla, P. M. W., Burton, W. B., Hartmann, D., et al. 2005, *A&A*, 440, 775

- Kereš, D., Katz, N., Fardal, M., Davé, R., & Weinberg, D. H. 2009, MNRAS, 395, 160
- Kwak, K., & Shelton, R. L. 2010, ApJ, 719, 523
- Lockman, F. J., Murphy, E. M., Petty-Powell, S., & Urick, V. 2002, ApJS, 140, 331
- Lockman, F. J., Benjamin, R. A., Heroux, A. J., & Langston, G. J. 2008, ApJ, 679, L21
- Moore, B., & Davis, M. 1994, MNRAS, 270, 209
- Morton, D. C. 2003, ApJS, 139, 205
- Osterman, S., Green, J., et al. 2011, Ap&SS, in press (arXiv:1012.5827)
- Pagel, B. E. J. 1994, in The Formation and Evolution of Galaxies, ed. C. Munez-Tunón & F. Sanchez (Cambridge: Cambridge Univ. Press), 149
- Reynolds, R. J. ApJ, 372, L17
- Richter, P., et al. 2001, ApJ, 559, 318
- Robitaille, T. P., & Whitney, B. A. 2010, ApJ, 710, L17
- Sembach, K. R., & Savage, B. D. 1992, ApJS, 83, 147
- Sembach, K. R., et al. 1999, ApJ, 515, 108
- Sembach, K. R., et al. 2003, ApJS, 146, 165
- Sembach, K. R., et al. 2004, ApJS, 150, 387
- Shull, J. M., Jones, J. R., Danforth, C. W., & Collins, J. A. 2009, ApJ, 699, 754
- Slavin, J. D., Shull, J. M., & Begelman, M. C. 1993, ApJ, 407, 83
- Spitzer, L. 1956, ApJ, 124, 20
- Spitzer, L. 1978, Physical Processes in the Interstellar Medium (New York: Wiley: Interscience)
- Thom, C., Peek, J. E. G., Putman, M. E., et al. 2008, ApJ, 684, 364
- Tremonti, C. A., et al. 2004, ApJ, 613, 898
- Tufte, S. L., Reynolds, R. J., & Haffner, L. M. 1998, ApJ, 504, 773
- van Woerden, H., Schwarz, U. J., Peltier, R. F., Wakker, B. P., & Kalberla, P. M. W. 1999, Nature, 400, 138
- Wakker, B. P., & van Woerden, H. 1997, ARA&A, 35, 217
- Wakker, B. P., et al. 1999, Nature, 402, 388
- Wakker, B. P. 2001, ApJS, 136, 463
- Wakker, B. P., et al. 2001, ApJS, 136, 537

Wakker, B. P., et al. 2007, ApJ, 670, L113

Wakker, B. P., Lockman, F. J., & Brown, J. M. 2011, ApJ, 728, 159

Winter, L. M. et al. 2011, ApJ, 728, 28

Yao, Y., Shull, J. M., & Danforth, C. W. 2011, ApJ, 728, L16

Table 1. COS Observations

Target ^a	Coordinates ^a	Program(s)	Grating	N_{exp}	t_{exp} (s)	$(S/N)_{\text{res}}$ ^b
Mrk 817	14:36:22.1 +58:47:39	11505, 11524	G130M	8	3426	41
$z = 0.031455$	$l = 100.30$, $b = 53.48$	11505, 11524	G160M	8	3010	35
Mrk 290	15:35:52.3 +57:54:09	11524	G130M	4	3857	22
$z = 0.029577$	$l = 91.49$, $b = 47.95$	11524	G160M	4	4801	22
Mrk 876	16:13:57.2 +65:43:10	11524, 11686	G130M	6	12580	57
$z = 0.12900$	$l = 98.27$, $b = 40.38$	11686	G160M	4	11820	37
PG 1259+593	13:01:13.1 +59:02:06	11541	G130M	4	9201	35
$z = 0.4778$	$l = 120.56$, $b = 58.05$	11541	G160M	4	11169	32

^aAGN target, redshifts and coordinates: RA/Decl (2000) and Galactic ℓ and b .

^bSignal-to-noise ratio per resolution element calculated at 1350 Å and 1550 Å for data with G130M (1132–1460 Å) and G160M (1394–1798 Å) gratings, respectively. The actual S/N values vary throughout each dataset, but the quoted values give a sense of relative data quality. See text for more details.

Table 2. Gaussian Fits^a to H I Column Densities

Target	$\langle V_{\text{LSR}} \rangle$ (km s ⁻¹)	Height (T_b (K))	FWHM (km s ⁻¹)	N_{HI} (in 10^{18} cm ⁻²)
Mrk 817	-108.0 ± 0.12	0.594 ± 0.0055	27.5 ± 0.3	31.7 ± 0.5
Mrk 290	-89.8 ± 1.2	0.310 ± 0.030	22.4 ± 1.3	13.5 ± 1.5
	-113.6 ± 0.5	0.583 ± 0.021	25.7 ± 2.8	29.1 ± 3.3
	-136.3 ± 0.26	1.608 ± 0.037	22.2 ± 0.3	69.4 ± 1.8
Mrk 876	-131.4 ± 0.3	0.381 ± 0.006	33.4 ± 0.7	24.7 ± 0.7
	-175.5 ± 0.8	0.116 ± 0.008	22.7 ± 1.9	5.1 ± 0.5
PG 1259+593	-126.4 ± 0.1	0.891 ± 0.061	12.0 ± 0.5	20.7 ± 1.6
	-129.1 ± 0.1	1.558 ± 0.062	24.1 ± 0.3	73.0 ± 3.1

^aGaussian components fitted to three parameters: LSR velocity (V_{LSR}), height (T_b), and full-width half-maximum (FWHM), from which we derive column density, $N_{\text{HI}} = (1.823 \times 10^{18} \text{ cm}^{-2})(\text{height})(\text{FWHM})(1.065)$, for height in units of T_b (K) and FWHM in km s⁻¹.

Table 3. HVC Measurements^a (Mrk 817)

Ion	λ_0 (Å)	V_c (km s ⁻¹)	b_{width} (km s ⁻¹)	W_λ (mÅ)	$\log N_a$ (N in cm ⁻²)
S II	1259.51	-104 ± 11	25 ± 7	42 ± 7	$14.29^{+0.08}_{-0.08}$
S II	1253.80	-102 ± 7	27 ± 9	19 ± 5	$14.12^{+0.12}_{-0.12}$
S II	1250.57	-123 ± 1	49 ± 14	27 ± 8	$14.57^{+0.15}_{-0.13}$
Si II	1526.70	-121 ± 5	43 ± 9	364 ± 66	$14.37^{+0.08}_{-0.07}$
Si II	1304.37	-114 ± 6	38 ± 6	241 ± 39	$14.47^{+0.08}_{-0.05}$
Si II	1193.28	-116 ± 6	41 ± 7	338 ± 61	$14.08^{+0.09}_{-0.07}$
Si II	1190.41	-116 ± 5	40 ± 8	295 ± 57	$14.23^{+0.10}_{-0.07}$
Fe II	1608.45	-113 ± 7	38 ± 6	173 ± 32	$14.23^{+0.10}_{-0.06}$
Fe II	1144.93	-113 ± 6	40 ± 7	117 ± 25	$14.19^{+0.11}_{-0.09}$
Fe II	1143.22	-117 ± 2	50 ± 17	49 ± 14	$14.40^{+0.17}_{-0.12}$
C II*	1335.66	-141 ± 5	55 ± 16	31 ± 15	$14.22^{+0.26}_{-0.19}$
C II	1334.53	-121 ± 5	43 ± 7	431 ± 75	$14.90^{+0.12}_{-0.12}$
N I	1200.71	-131 ± 1	42 ± 9	284 ± 44	$14.95^{+0.05}_{-0.04}$
N I	1200.22	-138 ± 2	47 ± 11	284 ± 68	$14.65^{+0.12}_{-0.08}$
N I	1199.54	-109 ± 5	36 ± 6	141 ± 27	$14.06^{+0.10}_{-0.07}$
O I	1302.16	-119 ± 5	42 ± 7	337 ± 57	$14.98^{+0.07}_{-0.06}$
Al II	1670.78	-119 ± 6	40 ± 7	404 ± 65	$13.23^{+0.07}_{-0.06}$
P II	1152.82	-117 ± 8	37 ± 9	23 ± 6	$12.95^{+0.09}_{-0.17}$
C IV	1550.78	-107 ± 9	37 ± 4	100 ± 24	$13.77^{+0.14}_{-0.09}$
C IV	1548.20	-107 ± 7	38 ± 6	170 ± 41	$13.75^{+0.14}_{-0.09}$
N V	1242.80	-119 ± 5	52 ± 10	13 ± 4	$13.08^{+0.12}_{-0.15}$
N V	1238.82	-109 ± 7	34 ± 10	31 ± 8	$13.16^{+0.10}_{-0.13}$
O VI	1031.93	-115 ± 7	43 ± 7	103 ± 27	$14.05^{+0.16}_{-0.09}$
Si III	1206.50	-118 ± 6	42 ± 8	355 ± 67	$13.74^{+0.15}_{-0.13}$
Si IV	1402.77	-106 ± 11	37 ± 5	56 ± 16	$13.15^{+0.15}_{-0.12}$
Si IV	1393.76	-109 ± 8	39 ± 9	91 ± 25	$13.08^{+0.13}_{-0.12}$

^aTable lists data for measured HVC absorption lines, including ion and rest wavelength, HVC velocity centroid (V_c), line width (b_{width}), equivalent width (W_λ), and column density (N_a) from apparent optical depth (AOD) integration. Error bars are 1σ , including both statistical errors in measurement and systematic effects of continuum placement and velocity range. For the HVC at $\langle V_{\text{LSR}} \rangle = -108$ km s⁻¹ our GBT measurements (Table 2) give $\log N_{\text{HI}} = 19.50 \pm 0.01$. Wakker et al. (2003) quote $\log N_{\text{HI}} = 19.51 \pm 0.01$.

Table 4. HVC Measurements (Mrk 290)

Ion	λ_0 (Å)	V_c (km s ⁻¹)	b_{width} (km s ⁻¹)	W_λ (mÅ)	$\log N_a$ (N in cm ⁻²)
$v_{\text{LSR}} \approx -120$ km s ⁻¹ Absorber ^a					
S II	1259.51	-123 ± 5	32 ± 5	55 ± 6	$14.43^{+0.05}_{-0.04}$
S II	1253.80	-115 ± 8	35 ± 10	11 ± 2	$13.93^{+0.06}_{-0.07}$
S II	1250.57	-104 ± 12	34 ± 4	83 ± 35	$15.14^{+0.26}_{-0.19}$
Si II	1526.70	-123 ± 2	37 ± 9	317 ± 64	$14.32^{+0.08}_{-0.06}$
Si II	1304.37	-118 ± 4	34 ± 6	207 ± 33	$14.40^{+0.09}_{-0.04}$
Si II	1193.28	-114 ± 5	34 ± 8	269 ± 59	$14.16^{+0.13}_{-0.07}$
Fe II	1608.45	-121 ± 3	35 ± 7	180 ± 28	$14.26^{+0.08}_{-0.05}$
Fe II	1144.93	-128 ± 4	38 ± 9	141 ± 30	$14.30^{+0.11}_{-0.09}$
C II*	1335.66	-120 ± 39	43 ± 17	< 15	$< 14.35(3\sigma)$
C II	1334.53	-122 ± 3	40 ± 12	389 ± 11	$14.85^{+0.50}_{-0.49}$
NI	1200.71	-127 ± 1	34 ± 7	212 ± 30	$14.82^{+0.06}_{-0.04}$
NI	1200.22	-135 ± 4	39 ± 11	210 ± 66	$14.51^{+0.19}_{-0.14}$
NI	1199.54	-119 ± 3	36 ± 8	144 ± 26	$14.06^{+0.10}_{-0.05}$
O I	1302.16	-130 ± 5	26 ± 4	187 ± 4	$14.64^{+0.03}_{-0.02}$
Al II	1670.78	-124 ± 4	38 ± 10	339 ± 83	$13.11^{+0.12}_{-0.09}$
P II	1152.82	-120 ± 25	45 ± 10	16 ± 4	$12.83^{+0.22}_{-0.18}$
C IV	1550.78	-118 ± 3	38 ± 12	104 ± 31	$13.79^{+0.13}_{-0.13}$
C IV	1548.20	-115 ± 5	37 ± 11	177 ± 54	$13.77^{+0.15}_{-0.13}$
N V	1242.80	-131 ± 17	50 ± 20	8 ± 4	$12.89^{+0.55}_{-0.18}$
N V	1238.82	-105 ± 1	37 ± 7	18 ± 7	$12.98^{+0.22}_{-0.15}$
O VI	1031.93	-124 ± 1	38 ± 11	113 ± 38	$14.10^{+0.15}_{-0.14}$
Si III	1206.50	-120 ± 1	40 ± 12	345 ± 96	$13.73^{+0.18}_{-0.15}$
Si IV	1402.77	-116 ± 3	39 ± 11	70 ± 19	$13.26^{+0.16}_{-0.10}$
Si IV	1393.76	-120 ± 2	41 ± 11	108 ± 33	$13.17^{+0.15}_{-0.12}$
$v_{\text{LSR}} \approx -220$ km s ⁻¹ Absorber ^b					
P II	1152.82	-225 ± 12	56 ± 5	< 15	$< 13.19(3\sigma)$
C IV	1550.78	-224 ± 1	33 ± 11	71 ± 17	$13.60^{+0.10}_{-0.12}$
C IV	1548.20	-223 ± 4	35 ± 5	110 ± 14	$13.51^{+0.08}_{-0.04}$
O VI	1031.93	-219 ± 8	33 ± 4	53 ± 14	$13.75^{+0.15}_{-0.22}$
Si IV	1402.77	-218 ± 2	33 ± 12	35 ± 8	$12.95^{+0.12}_{-0.13}$
Si IV	1393.76	-218 ± 7	32 ± 7	69 ± 12	$12.96^{+0.07}_{-0.09}$

Table 4—Continued

Ion	λ_0 (Å)	V_c (km s ^{−1})	b_{width} (km s ^{−1})	W_λ (mÅ)	$\log N_a$ (N in cm ^{−2})
Si III	1206.50	-211 ± 7	31 ± 5	180 ± 38	$13.15^{+0.10}_{-0.08}$

^aTable lists data for measured HVC absorption lines, including ion and rest wavelength, HVC velocity centroid (V_c), line width (b_{width}), equivalent width (W_λ), and column density (N_a) from apparent optical depth (AOD) integration. Error bars are 1σ , including both statistical errors in measurement and systematic effects of continuum placement and velocity range. For the composite UV absorber at $\langle V_{\text{LSR}} \rangle = -120$ km s^{−1}, our GBT measurements (Table 2) give $\log N_{\text{HI}} = 20.05 \pm 0.02$ for components at $V_{\text{LSR}} = -136, -113$, and -90 km s^{−1}. Wakker et al. (2003) measure a combined $\log N_{\text{HI}} = 20.10 \pm 0.02$ for HVCs at -134 km s^{−1} and -105 km s^{−1}.

^bFor the UV-only absorber at $\langle V_{\text{LSR}} \rangle = -220$ km s^{−1} Wakker et al. (2003) find no H I emission to a limit $\log N_{\text{HI}} < 18.3$. Our GBT limit over the range (-275 to -175 km s^{−1}) is $\log N_{\text{HI}} < 18.0$ (at 4σ).

Table 5. HVC Measurements^a (Mrk 876)

Ion	λ_0 (Å)	V_c (km s ⁻¹)	b_{width} (km s ⁻¹)	W_λ (mÅ)	$\log N_a$ (N in cm ⁻²)
$v_{\text{LSR}} \approx -133$ km s ⁻¹ Absorber ^a					
S II	1259.51	-132 ± 3	25 ± 10	37 ± 13	$14.24^{+0.16}_{-0.13}$
S II	1253.80	-133 ± 2	24 ± 11	25 ± 8	$14.25^{+0.13}_{-0.14}$
S II	1250.57	-137 ± 3	24 ± 10	16 ± 5	$14.37^{+0.14}_{-0.13}$
Si II	1526.70	-135 ± 1	26 ± 10	259 ± 86	$14.30^{+0.14}_{-0.08}$
Si II	1304.37	-134 ± 1	26 ± 11	191 ± 65	$14.41^{+0.16}_{-0.09}$
Si II	1193.28	-134 ± 1	28 ± 12	242 ± 100	$13.97^{+0.19}_{-0.12}$
Si II	1190.41	-133 ± 1	27 ± 12	227 ± 90	$14.19^{+0.18}_{-0.11}$
Fe II	1608.45	-136 ± 1	26 ± 11	168 ± 56	$14.26^{+0.17}_{-0.10}$
Fe II	1144.93	-134 ± 2	27 ± 11	118 ± 43	$14.24^{+0.18}_{-0.12}$
Fe II	1143.22	-140 ± 2	24 ± 6	34 ± 6	$14.25^{+0.13}_{-0.06}$
Fe II	1133.67	-132 ± 4	29 ± 8	31 ± 13	$14.83^{+0.27}_{-0.15}$
P II	1152.82	-130 ± 1	29 ± 12	24 ± 10	$12.97^{+0.32}_{-0.12}$
C II*	1335.66	-137 ± 7	26 ± 13	14 ± 8	$13.86^{+0.21}_{-0.24}$
C II	1334.53	-134 ± 1	28 ± 13	292 ± 134	$14.79^{+0.24}_{-0.16}$
NI	1200.71	-139 ± 3	26 ± 10	213 ± 78	$14.99^{+0.19}_{-0.11}$
NI	1200.22	-142 ± 4	26 ± 11	148 ± 68	$14.36^{+0.26}_{-0.23}$
NI	1199.54	-134 ± 2	24 ± 9	112 ± 32	$13.97^{+0.13}_{-0.08}$
O I	1302.16	-136 ± 1	26 ± 11	206 ± 79	$14.74^{+0.16}_{-0.12}$
Al II	1670.78	-137 ± 1	27 ± 12	280 ± 105	$13.12^{+0.17}_{-0.11}$
C IV	1550.78	-130 ± 3	29 ± 13	73 ± 37	$13.63^{+0.31}_{-0.18}$
C IV	1548.20	-129 ± 2	29 ± 12	117 ± 57	$13.58^{+0.29}_{-0.18}$
N V	1242.80	-135 ± 1	28 ± 15	7 ± 4	$12.82^{+0.18}_{-0.29}$
N V	1238.82	-139 ± 2	27 ± 14	14 ± 6	$12.85^{+0.23}_{-0.14}$
O VI	1031.93	-136 ± 1	30 ± 13	86 ± 43	$13.99^{+0.36}_{-0.14}$
Si IV	1402.77	-128 ± 4	28 ± 11	48 ± 20	$13.09^{+0.24}_{-0.14}$
Si IV	1393.76	-129 ± 3	24 ± 11	91 ± 39	$13.10^{+0.25}_{-0.15}$
Si III	1206.50	-134 ± 1	29 ± 12	269 ± 117	$13.72^{+0.24}_{-0.14}$
$v_{\text{LSR}} \approx -190$ km s ⁻¹ Absorber ^b					
Si III	1206.50	-198 ± 8	27 ± 7	162 ± 59	$13.17^{+0.21}_{-0.19}$
Si II	1526.70	-197 ± 8	24 ± 6	129 ± 42	$13.81^{+0.13}_{-0.18}$
Si II	1304.37	-200 ± 8	31 ± 6	87 ± 30	$13.92^{+0.17}_{-0.15}$

Table 5—Continued

Ion	λ_0 (Å)	V_c (km s ⁻¹)	b_{width} (km s ⁻¹)	W_λ (mÅ)	$\log N_a$ (N in cm ⁻²)
Si II	1193.28	-196 ± 8	25 ± 5	145 ± 49	$13.56^{+0.21}_{-0.13}$
Si II	1190.41	-196 ± 7	27 ± 7	118 ± 42	$13.69^{+0.21}_{-0.14}$
Fe II	1608.45	-200 ± 9	30 ± 9	77 ± 32	$13.84^{+0.17}_{-0.20}$
Fe II	1144.93	-200 ± 4	33 ± 14	40 ± 21	$13.68^{+0.22}_{-0.23}$
O I	1302.16	-199 ± 7	28 ± 6	165 ± 47	$14.57^{+0.15}_{-0.12}$
Al II	1670.78	-202 ± 9	30 ± 6	151 ± 54	$12.64^{+0.14}_{-0.22}$
C IV	1550.78	-191 ± 14	18 ± 3	25 ± 12	$13.13^{+0.15}_{-0.12}$
C IV	1548.20	-192 ± 10	27 ± 5	43 ± 19	$13.09^{+0.25}_{-0.17}$
Si IV	1402.77	-188 ± 20	13 ± 8	11 ± 3	$12.40^{+0.25}_{-0.12}$
Si IV	1393.76	-195 ± 6	34 ± 13	22 ± 13	$12.44^{+0.31}_{-0.24}$

^aTable lists data for measured HVC absorption lines, including ion and rest wavelength, HVC velocity centroid (V_c), line width (b_{width}), equivalent width (W_λ), and column density (N_a) from apparent optical depth (AOD) integration. Error bars are 1σ , including both statistical errors in measurement and systematic effects of continuum placement and velocity range. Our GBT measurements give $\log N_{\text{HI}} = 19.39 \pm 0.01$ and $\log N_{\text{HI}} = 18.71 \pm 0.04$ for HVC components at $V_{\text{LSR}} = -131$ km s⁻¹ and -175 km s⁻¹, respectively (Table 2). Wakker et al. (2003) measure $\log N_{\text{HI}} = 19.30 \pm 0.02$ at $V_{\text{LSR}} = -133$ km s⁻¹.

^bFor this UV-only HVC, our GBT measurements (Table 2) give $\log N_{\text{HI}} = 18.71 \pm 0.04$ at $V_{\text{LSR}} = -175$ km s⁻¹. Wakker et al. (2003) report no HI emission at -190 km s⁻¹, but they find $\log N_{\text{HI}} = 18.67 \pm 0.08$ for a weak component at $V_{\text{LSR}} = -173$ km s⁻¹.

Table 6. HVC Measurements^a (PG 1259+593)

Ion	λ_0 (Å)	V_c (km s ⁻¹)	b_{width} (km s ⁻¹)	W_λ (mÅ)	$\log N_a$ (N in cm ⁻²)
S II	1259.51	-127 ± 6	23 ± 7	38 ± 10	$14.27^{+0.11}_{-0.11}$
S II	1253.80	-128 ± 5	25 ± 9	30 ± 8	$14.35^{+0.15}_{-0.10}$
S II	1250.57	-120 ± 8	18 ± 1	22 ± 5	$14.51^{+0.11}_{-0.10}$
Si II	1526.70	-124 ± 6	25 ± 9	188 ± 62	$14.06^{+0.14}_{-0.15}$
Si II	1304.37	-124 ± 6	22 ± 8	126 ± 39	$14.17^{+0.10}_{-0.14}$
Si II	1193.28	-121 ± 7	24 ± 7	166 ± 55	$13.66^{+0.19}_{-0.15}$
Si II	1190.41	-122 ± 5	25 ± 9	160 ± 56	$13.90^{+0.17}_{-0.14}$
Fe II	1608.45	-126 ± 7	24 ± 7	123 ± 34	$14.11^{+0.12}_{-0.11}$
Fe II	1144.93	-126 ± 6	29 ± 12	97 ± 39	$14.13^{+0.22}_{-0.16}$
Fe II	1143.22	-138 ± 0	19 ± 14	26 ± 5	$14.16^{+0.11}_{-0.12}$
P II	1152.82	-130 ± 3	13 ± 28	< 10	$< 13.02(3\sigma)$
C II*	1335.66	-140 ± 13	33 ± 8	35 ± 24	$14.29^{+0.34}_{-0.31}$
C II	1334.53	-122 ± 5	26 ± 9	219 ± 75	$14.45^{+0.23}_{-0.17}$
N I	1200.71	-130 ± 1	30 ± 12	193 ± 77	$14.79^{+0.21}_{-0.14}$
N I	1200.22	-140 ± 3	27 ± 12	167 ± 67	$14.44^{+0.23}_{-0.14}$
N I	1199.54	-127 ± 5	24 ± 9	89 ± 26	$13.85^{+0.12}_{-0.12}$
Al II	1670.78	-127 ± 5	26 ± 9	214 ± 69	$12.89^{+0.13}_{-0.16}$
C IV	1550.78	-124 ± 9	27 ± 8	25 ± 10	$13.13^{+0.24}_{-0.16}$
C IV	1548.20	-115 ± 8	23 ± 7	41 ± 19	$13.08^{+0.33}_{-0.15}$
N V	1242.80	-125 ± 6	31 ± 13	< 14	$< 13.59(3\sigma)$
N V	1238.82	-122 ± 9	23 ± 10	< 7	$< 12.99(3\sigma)$
O VI	1031.93	-130 ± 3	27 ± 8	39 ± 13	$13.58^{+0.10}_{-0.12}$
Si IV	1402.77	-119 ± 4	25 ± 11	23 ± 9	$12.75^{+0.22}_{-0.16}$
Si IV	1393.76	-124 ± 6	26 ± 8	34 ± 12	$12.64^{+0.17}_{-0.13}$
Si III	1206.50	-124 ± 6	27 ± 8	187 ± 67	$13.30^{+0.24}_{-0.16}$

^aTable lists data for measured HVC absorption lines, including ion and rest wavelength, HVC velocity centroid (V_c), line width (b_{width}), equivalent width (W_λ), and column density (N_a) from apparent optical depth (AOD) integration. Error bars are 1σ , including both statistical errors in measurement and systematic effects of continuum placement and velocity range. The GBT measurements give $\log N_{\text{HI}} = 19.97 \pm 0.02$ for the two-component HVC (-126.4 km s⁻¹ and $= 129.1$ km s⁻¹) at $\langle V_{\text{LSR}} \rangle = -128$ km s⁻¹. Wakker et al. (2003) measure $\log N_{\text{HI}} = 19.95 \pm 0.01$ for an HVC at $V_{\text{LSR}} = -128$ km s⁻¹, and Sembach et al. (2004) adopt $\log N_{\text{HI}} = 19.94 \pm 0.06$ for this HVC.

Table 7. Mrk 817: Summary Column Densities^a and Abundances

Species (X_i)	CSG-03 ($\log N_{X_i}$)	Shull-11 ($\log N_{X_i}$)	Adopted ($\log N_{X_i}$)	Abundance ^b $\log(N_{X_i}/N_{\text{HI}})$	Abundance ^b [X/H]
O I	$15.72^{+0.24}_{-0.16}$	≥ 14.98	$15.72^{+0.24}_{-0.16}$	-3.78 ± 0.24	-0.47 ± 0.24
N I	< 14.05	$14.06^{+0.12}_{-0.07}$	$14.06^{+0.12}_{-0.07}$	-5.44 ± 0.10	-1.27 ± 0.10
S II	$14.34^{+0.05}_{-0.05}$	$14.29^{+0.08}_{-0.08}$	$14.29^{+0.08}_{-0.08}$	-5.21 ± 0.08	-0.60 ± 0.10
Si II	$14.48^{+0.07}_{-0.08}$	$14.47^{+0.08}_{-0.05}$	$14.47^{+0.08}_{-0.05}$	-5.03 ± 0.08	-0.75 ± 0.10
Fe II	$14.31^{+0.11}_{-0.08}$	$14.23^{+0.10}_{-0.06}$	$14.23^{+0.10}_{-0.06}$	-5.27 ± 0.10	-0.88 ± 0.15
C II	...	≥ 14.9	≥ 14.9	> -4.6	≥ -1.03
Al II	...	$13.23^{+0.07}_{-0.06}$	$13.23^{+0.07}_{-0.06}$	-6.27 ± 0.07	-0.72 ± 0.07
P II	...	< 12.95	< 12.95	< -6.55	< 0.04
C IV	...	$13.77^{+0.14}_{-0.09}$	$13.77^{+0.14}_{-0.09}$	$-5.73^{+0.14}_{-0.09}$	
N V	...	$13.16^{+0.10}_{-0.13}$	$13.16^{+0.10}_{-0.13}$	$-6.34^{+0.10}_{-0.13}$	
O VI	...	$14.05^{+0.16}_{-0.09}$	$14.05^{+0.16}_{-0.09}$	$-5.45^{+0.16}_{-0.09}$	
Si IV	...	$13.08^{+0.13}_{-0.12}$	$13.08^{+0.13}_{-0.12}$	$-6.42^{+0.13}_{-0.12}$	
Si III	...	$13.74^{+0.15}_{-0.13}$	$13.74^{+0.15}_{-0.13}$	$-5.76^{+0.15}_{-0.13}$	

^aComparison of measured column densities, $\log N_a(\text{cm}^{-2})$, for HVC at $\langle V_{\text{LSR}} \rangle = -109 \text{ km s}^{-1}$ (integrated from -190 km s^{-1} to -70 km s^{-1}).

^bAbundances for neutrals and first ions X_i are given relative to measured $\log N_{\text{HI}} = 19.50 \pm 0.01$ (Table 2). Fox et al. (2004) found $\log N(\text{O VI}) = 13.97^{+0.10}_{-0.13}$ for HVC absorption between -160 and -80 km s^{-1} . Last column gives abundances of elements [X/H] relative to solar abundances (Asplund et al. 2009), with ionization corrections of 0.27 dex (S II), 0.21 dex (Si II), and 0.11 dex (Fe II) subtracted from the first-ion abundances (Section 3.2).

Table 8. Mrk 290: Summary Column Densities^a and Abundances

Species (X_i)	CSG-03 ($\log N_{X_i}$)	CSG-07 ($\log N_{X_i}$)	Shull-11 ($\log N_{X_i}$)	Adopted ($\log N_{X_i}$)	Abundance ^b $\log(N_{X_i}/N_{\text{HI}})$	Abundance ^b [X/H]
O I	< 16.79	$15.75^{+0.29}_{-0.15}$	$14.64^{+0.03}_{-0.02}$	$15.75^{+0.29}_{-0.15}$	$-4.30^{+0.29}_{-0.15}$	$-0.99^{+0.29}_{-0.15}$
NI	< 15.02	$14.23^{+0.17}_{-0.20}$	$14.06^{+0.12}_{-0.07}$	$14.06^{+0.12}_{-0.07}$	$-5.99^{+0.12}_{-0.07}$	$-1.82^{+0.12}_{-0.07}$
S II	$14.29^{+0.15}_{-0.14}$	$14.24^{+0.16}_{-0.20}$	$14.43^{+0.08}_{-0.08}$	$14.43^{+0.08}_{-0.08}$	$-5.62^{+0.08}_{-0.08}$	$-0.78^{+0.15}_{-0.15}$
Si II	< 14.97	$14.93^{+0.18}_{-0.13}$	> 14.40	$14.93^{+0.18}_{-0.13}$	$-5.12^{+0.18}_{-0.13}$	$-0.67^{+0.15}_{-0.15}$
Fe II	< 15.46	$14.41^{+0.23}_{-0.21}$	$14.26^{+0.09}_{-0.05}$	$14.26^{+0.09}_{-0.05}$	$-5.79^{+0.09}_{-0.05}$	$-1.31^{+0.09}_{-0.05}$
Al II	$13.11^{+0.12}_{-0.09}$	$13.11^{+0.12}_{-0.09}$	$-6.94^{+0.12}_{-0.09}$	$-1.39^{+0.12}_{-0.09}$
P II	...	< 12.82	$12.83^{+0.22}_{-0.18}$	$12.83^{+0.22}_{-0.18}$	$-7.22^{+0.22}_{-0.18}$	$-0.63^{+0.22}_{-0.18}$
C IV	$13.78^{+0.14}_{-0.09}$	$13.78^{+0.14}_{-0.09}$	$-6.27^{+0.14}_{-0.09}$	
N V	...	< 13.49	$12.98^{+0.22}_{-0.15}$	$12.98^{+0.22}_{-0.15}$	$-7.07^{+0.22}_{-0.15}$	
O VI	...	$14.23^{+0.04}_{-0.04}$	$14.10^{+0.15}_{-0.14}$	$14.10^{+0.15}_{-0.14}$	$-5.95^{+0.15}_{-0.14}$	
Si IV	$12.95^{+0.12}_{-0.12}$	$12.95^{+0.12}_{-0.12}$	$-7.10^{+0.12}_{-0.12}$	
Si III	$13.15^{+0.10}_{-0.08}$	$13.15^{+0.10}_{-0.08}$	$-6.90^{+0.10}_{-0.08}$	

^aComparison of measured column densities, $\log N_a(\text{cm}^{-2})$, for HVC at $\langle V_{\text{LSR}} \rangle = -120 \text{ km s}^{-1}$ (integrated from -175 km s^{-1} to -75 km s^{-1}).

^bAbundances for neutrals and first ions X_i are given relative to measured $\log N_{\text{HI}} = 20.05 \pm 0.02$ for all three HVC components (Table 2). Wakker et al. (1999) found $\log N(\text{S II}) = 14.34^{+0.08}_{-0.11}$. Last column gives elemental abundances $[X/H]$ relative to solar values (Asplund et al. 2009) with ionization corrections of 0.04 dex (S II), 0.04 dex (Si II), and 0.02 dex (Fe II) subtracted from the first-ion abundances (Section 3.2).

Table 9. Mrk 876: Summary Column Densities^a and Abundances

Species (X_i)	CSG-03 ($\log N_{X_i}$)	CSG-07 ($\log N_{X_i}$)	Shull-11 ($\log N_{X_i}$)	Adopted ($\log N_{X_i}$)	Abundance ^b $\log(N_{X_i}/N_{\text{HI}})$	Abundance ^b [X/H]
O I	$15.55^{+0.42}_{-0.28}$	$15.26^{+0.17}_{-0.14}$	> 14.74	$15.26^{+0.17}_{-0.14}$	$-4.13^{+0.17}_{-0.14}$	$-0.82^{+0.17}_{-0.14}$
N I	$14.20^{+0.15}_{-0.14}$	$13.90^{+0.03}_{-0.04}$	$13.97^{+0.13}_{-0.08}$	$13.97^{+0.13}_{-0.08}$	$-5.42^{+0.13}_{-0.08}$	$-1.25^{+0.13}_{-0.08}$
S II	...	< 14.34	$14.25^{+0.13}_{-0.14}$	$14.25^{+0.13}_{-0.14}$	$-5.14^{+0.13}_{-0.14}$	$-0.58^{+0.20}_{-0.20}$
Si II	$14.53^{+0.11}_{-0.13}$	$14.56^{+0.11}_{-0.09}$	$14.41^{+0.16}_{-0.09}$	$14.41^{+0.16}_{-0.09}$	$-4.98^{+0.13}_{-0.14}$	$-0.76^{+0.20}_{-0.20}$
Fe II	$14.41^{+0.09}_{-0.08}$	$14.36^{+0.07}_{-0.07}$	$14.26^{+0.17}_{-0.10}$	$14.26^{+0.17}_{-0.10}$	$-5.13^{+0.17}_{-0.10}$	$-0.77^{+0.20}_{-0.20}$
C II	> 14.76	> 14.79	> -4.60	> -1.03
Al II	...	$13.43^{+0.31}_{-0.19}$	$13.12^{+0.07}_{-0.11}$	$13.12^{+0.17}_{-0.11}$	$-6.27^{+0.17}_{-0.11}$	$-0.72^{+0.20}_{-0.20}$
P II	< 13.21	...	< 12.97	< 12.97	< -6.42	< 0.13
C IV	...	$13.80^{+0.04}_{-0.03}$	$13.58^{+0.29}_{-0.18}$	$13.58^{+0.29}_{-0.18}$	$-5.81^{+0.29}_{-0.18}$	
N V	...	< 13.32	$12.85^{+0.23}_{-0.14}$	$12.85^{+0.23}_{-0.14}$	$-6.54^{+0.23}_{-0.14}$	
O VI	...	$14.20^{+0.02}_{-0.02}$	$13.99^{+0.36}_{-0.14}$	$13.99^{+0.36}_{-0.14}$	$-5.40^{+0.36}_{-0.14}$	
Si IV	...	$13.28^{+0.03}_{-0.02}$	$13.10^{+0.25}_{-0.15}$	$13.10^{+0.25}_{-0.15}$	$-6.29^{+0.25}_{-0.15}$	
Si III	$13.72^{+0.24}_{-0.14}$	$13.72^{+0.24}_{-0.14}$	$-5.67^{+0.24}_{-0.14}$	

^aComparison of measured column densities, $\log N_a(\text{cm}^{-2})$, for HVC at $\langle V_{\text{LSR}} \rangle = -133 \text{ km s}^{-1}$ (integrated from -170 km s^{-1} to -100 km s^{-1}).

^bAbundances for neutrals and first ions X_i are given relative to measured $\log N_{\text{HI}} = 19.39 \pm 0.01$ for the -131 km s^{-1} component (Table 2). Fox et al. (2004) found $\log N(\text{O VI}) = 14.12^{+0.11}_{-0.13}$ and $\log N(\text{N V}) < 13.43$. Our previous Si III survey (Shull et al. 2009) measured $\log N(\text{Si III}) \geq 13.92$ as adopted here. Last column gives elemental abundances $[X/H]$ relative to solar values (Asplund et al. 2009), with ionization corrections of 0.32 dex (S II), 0.27 dex (Si II), and 0.14 dex (Fe II) subtracted from the first-ion abundances (Section 3.2).

Table 10. PG1259+593: Summary Column Densities and Abundances^a

Species (X_i)	CSG-03 ($\log N_{X_i}$)	Richter-01 ($\log N_{X_i}$)	Shull-11 ($\log N_{X_i}$)	Adopted ($\log N_{X_i}$)	Abundance ^b $\log(N_{X_i}/N_{\text{HI}})$	Abundance ^b [X/H]
O I	$15.75^{+0.18}_{-0.24}$	$15.77^{+0.37}_{-0.31}$...	$15.85^{+0.15}_{-0.15}$	$-4.12^{+0.15}_{-0.15}$	$-0.81^{+0.15}_{-0.15}$
N I	$14.02^{+0.19}_{-0.12}$	$13.95^{+0.17}_{-0.21}$	$13.85^{+0.12}_{-0.12}$	$13.85^{+0.12}_{-0.12}$	$-6.12^{+0.12}_{-0.12}$	$-1.95^{+0.12}_{-0.12}$
S II	$14.38^{+0.12}_{-0.11}$	$14.34^{+0.12}_{-0.15}$	$14.35^{+0.15}_{-0.10}$	$14.35^{+0.15}_{-0.10}$	$-5.62^{+0.15}_{-0.10}$	$-0.78^{+0.15}_{-0.10}$
Si II	$14.67^{+0.20}_{-0.15}$	$14.56^{+0.28}_{-0.27}$	$14.17^{+0.10}_{-0.14}$	$14.17^{+0.10}_{-0.14}$	$-5.80^{+0.10}_{-0.14}$	$-1.35^{+0.10}_{-0.14}$
Fe II	$14.40^{+0.17}_{-0.08}$	$14.16^{+0.20}_{-0.14}$	$14.11^{+0.12}_{-0.11}$	$14.11^{+0.12}_{-0.11}$	$-5.86^{+0.12}_{-0.11}$	$-1.38^{+0.12}_{-0.11}$
C II	> 14.45	> 14.45	> -5.52	> -1.95
Al II	$13.45^{+0.17}_{-0.16}$	$13.42^{+0.30}_{-0.50}$	$12.89^{+0.13}_{-0.16}$	$12.89^{+0.13}_{-0.16}$	$-7.08^{+0.13}_{-0.16}$	$-1.53^{+0.13}_{-0.16}$
P II	< 12.96	< 13.22	< 12.43	< 12.43	< -7.54	< -0.95
C IV	$13.08^{+0.33}_{-0.15}$	$13.08^{+0.33}_{-0.15}$	$-6.89^{+0.33}_{-0.15}$	
N V	< 12.99	< 12.99	< -6.98	
O VI	$13.58^{+0.18}_{-0.12}$	$13.58^{+0.18}_{-0.12}$	$-6.39^{+0.18}_{-0.12}$	
Si IV	$12.64^{+0.17}_{-0.13}$	$12.64^{+0.17}_{-0.13}$	$-7.33^{+0.17}_{-0.13}$	
Si III	$13.30^{+0.24}_{-0.16}$	$13.30^{+0.24}_{-0.16}$	$-6.67^{+0.24}_{-0.16}$	

^aComparison of measured column densities, $\log N_a(\text{cm}^{-2})$, for HVC at $\langle V_{\text{LSR}} \rangle = -128 \text{ km s}^{-1}$ (integrated from -170 to -95 km s^{-1}).

^bAbundances for neutrals and first ions X_i are given relative to measured $\log N_{\text{HI}} = 19.97 \pm 0.02$ for the HVC components at -126 km s^{-1} and -129 km s^{-1} (Table 2). We adopted $\log N_{\text{OI}} = 15.85 \pm 0.15$ from Sembach et al. (2004). Fox et al. (2004) found $\log N(\text{C IV}) = 13.26^{+0.04}_{-0.06}$, $\log N(\text{N V}) < 12.85$, $\log N(\text{Si IV}) = 12.73^{+0.05}_{-0.03}$, $\log N(\text{O VI}) = 13.71^{+0.09}_{-0.09}$. Our previous Si III survey (Shull et al. 2009) measured $\log N(\text{Si III}) \geq 13.60$ as adopted here. Last column gives elemental abundances $[X/H]$ relative to solar values (Asplund et al. 2009), with ionization corrections of 0.04 dex (S II), 0.04 dex (Si II), and 0.02 dex (Fe II) subtracted from the first-ion abundances (Section 3.2).

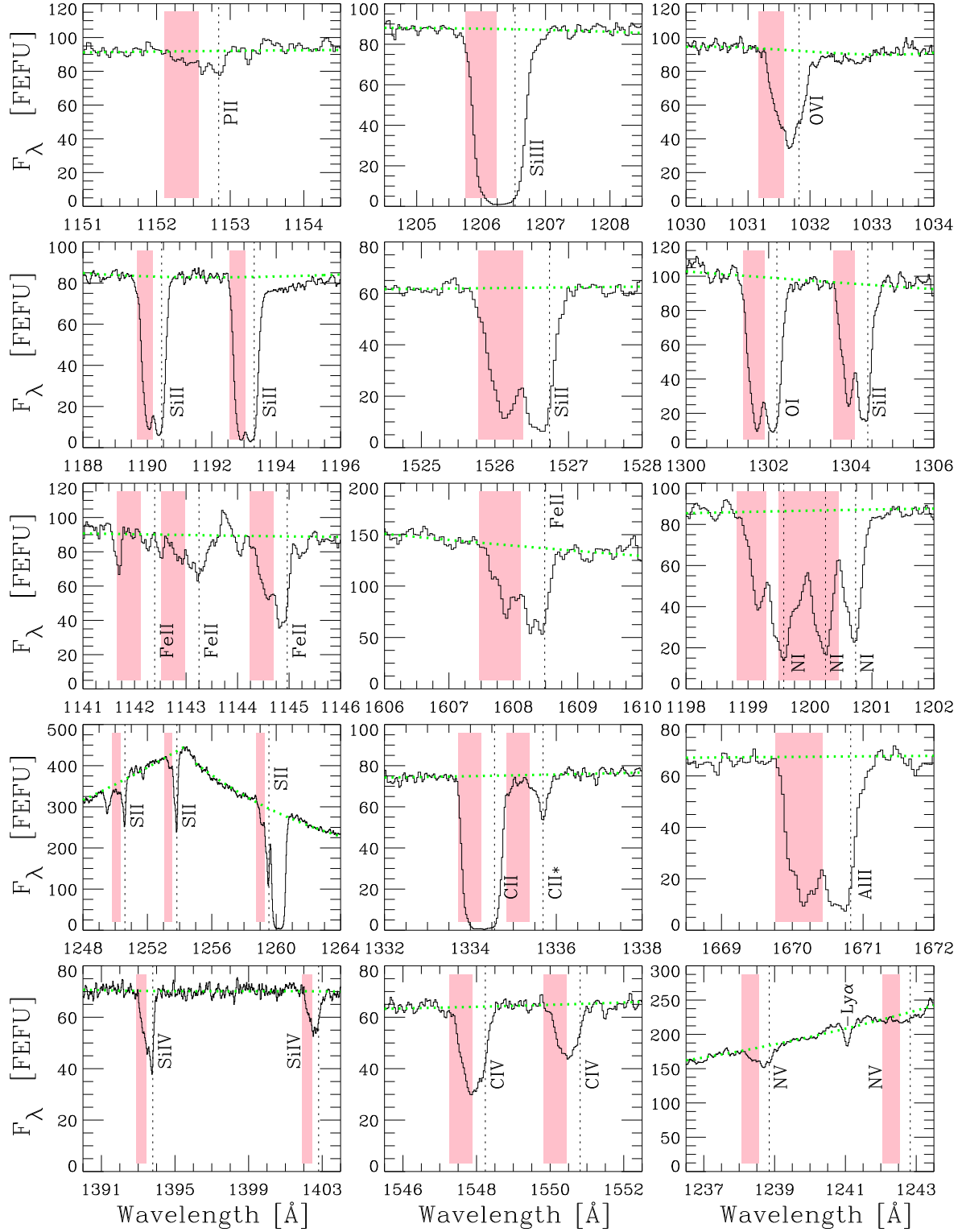


Fig. 4.— Detail of COS (G130M, G160M) data on HVC at $\langle V_{\text{LSR}} \rangle = -109 \text{ km s}^{-1}$ (range -190 to -70 km s^{-1}) toward Mrk 817, showing absorption lines of both low and high ions. HVC Complex C is seen in UV absorption indicated by pink wash. Fluxes are shown in FEFU (femto-erg flux units) or $10^{-15} \text{ erg cm}^{-2} \text{ s}^{-1} \text{ \AA}^{-1}$.

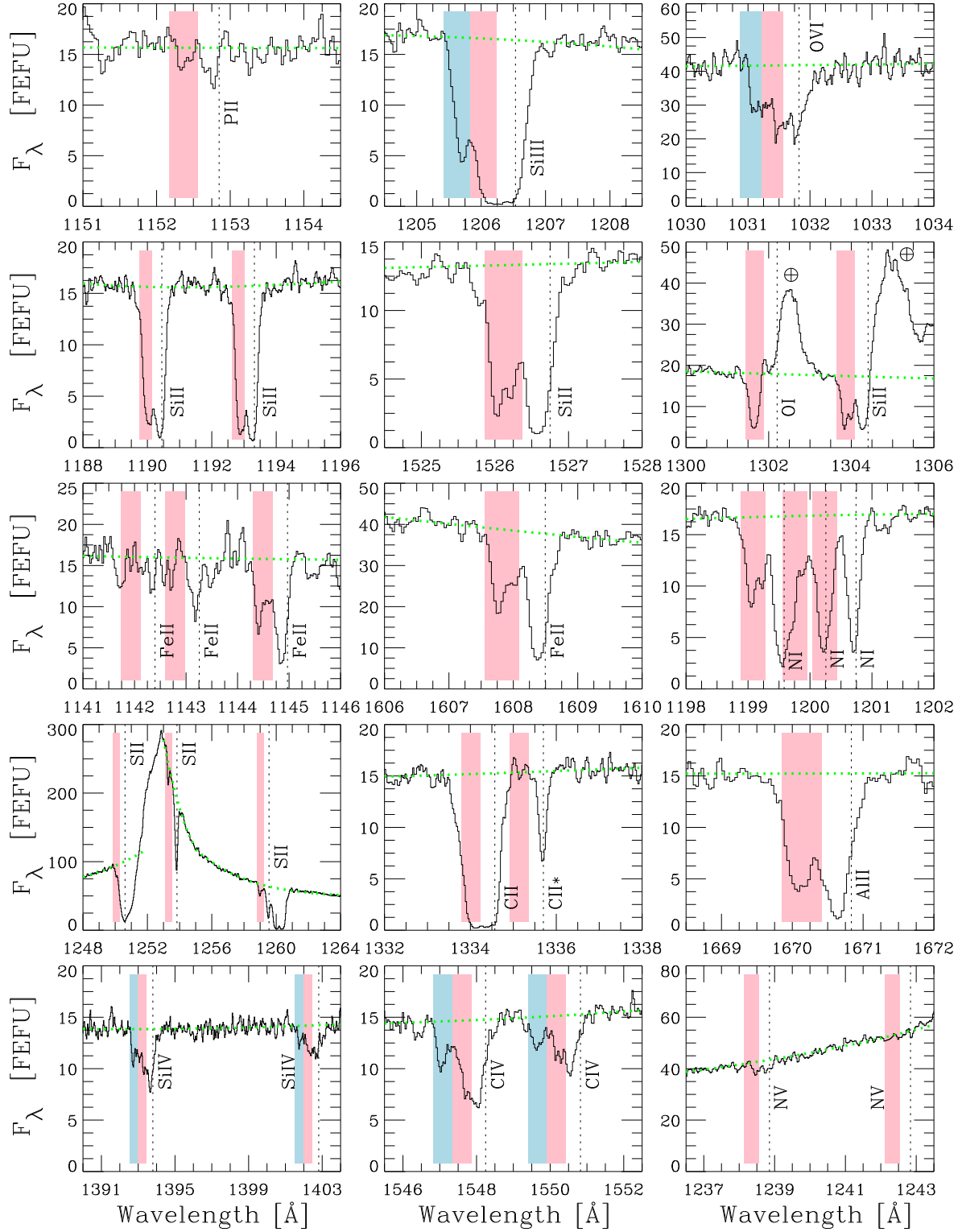


Fig. 5.— Same as Fig. 4 for Mrk 290 sight line. Note two HVCs shown by pink and blue wash, corresponding to components at $\langle V_{\text{LSR}} \rangle = -120 \text{ km s}^{-1}$ (range -175 to -75 km s^{-1}) and $\langle V_{\text{LSR}} \rangle = -220 \text{ km s}^{-1}$ (range -275 to -175 km s^{-1}).

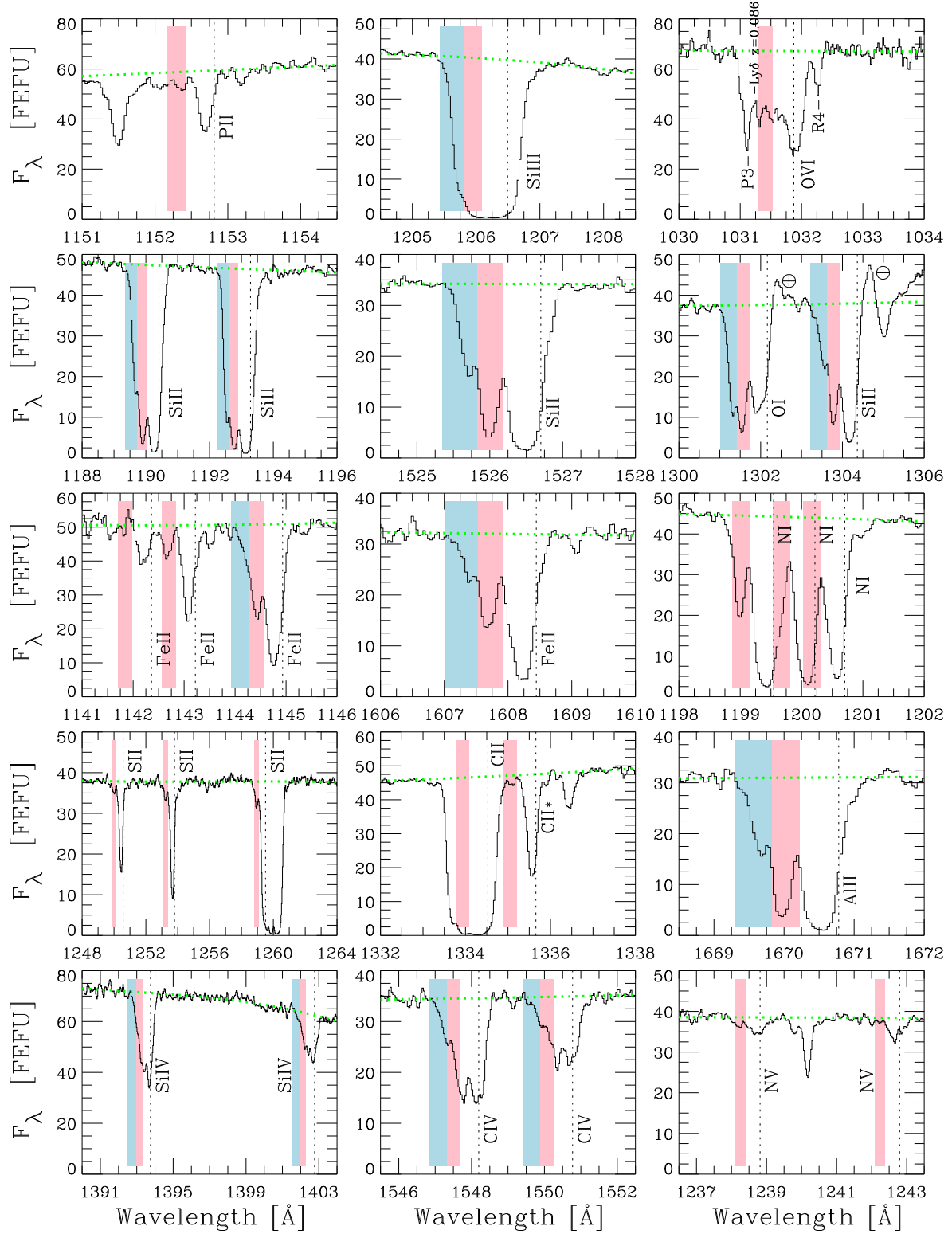


Fig. 6.— Same as Fig. 4 for Mrk 876 sight line. Note two HVCs shown by pink and blue wash, corresponding to components at $\langle V_{\text{LSR}} \rangle = -133 \text{ km s}^{-1}$ (range -170 to -100 km s^{-1}) and $\langle V_{\text{LSR}} \rangle = -190 \text{ km s}^{-1}$ (range -265 to -160 km s^{-1}).

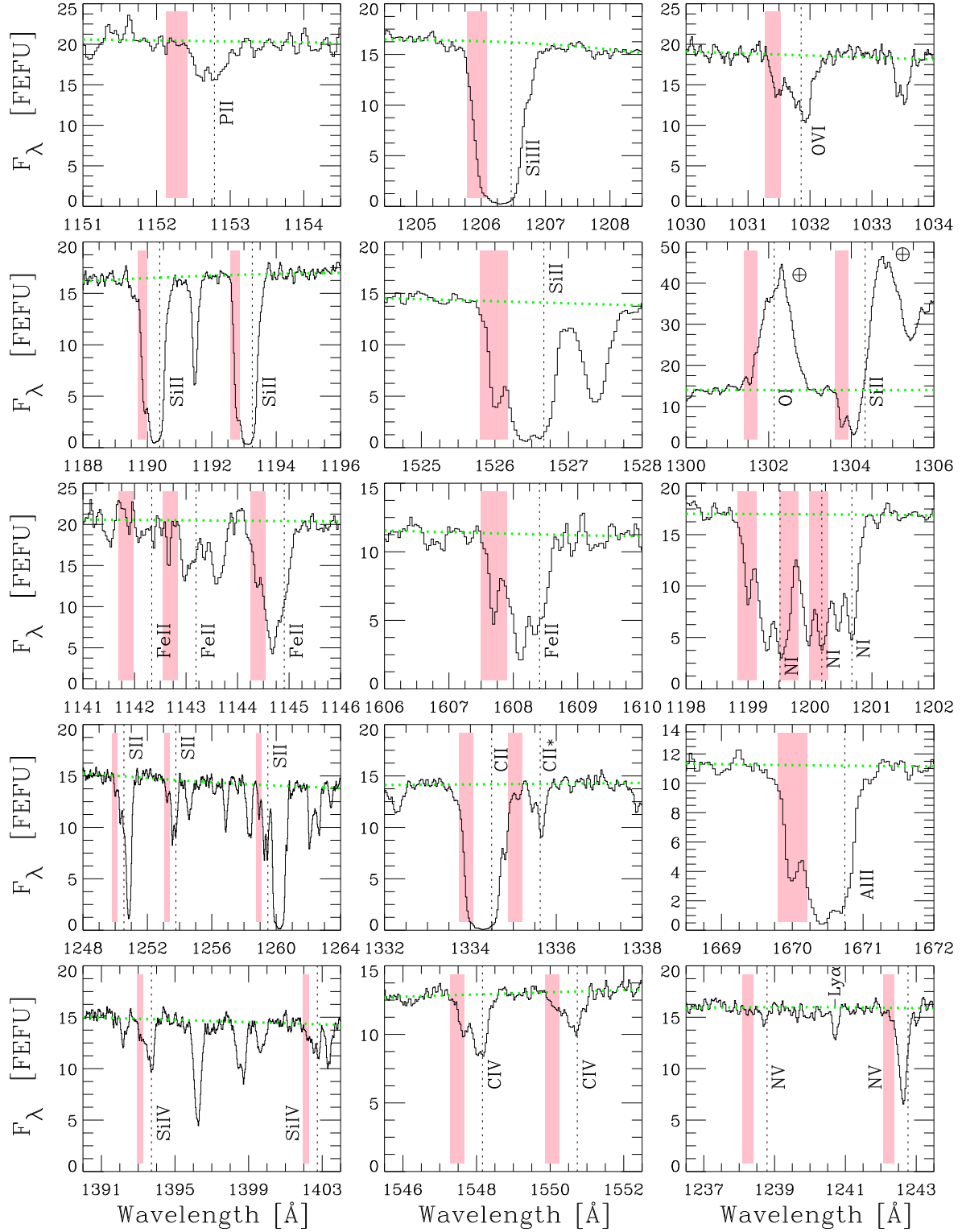


Fig. 7.— Same as Fig. 4 for PG 1259+593 sight line. Complex C (pink wash) is seen at $\langle V_{\text{LSR}} \rangle = -128 \text{ km s}^{-1}$ (range -170 to -95 km s^{-1}).

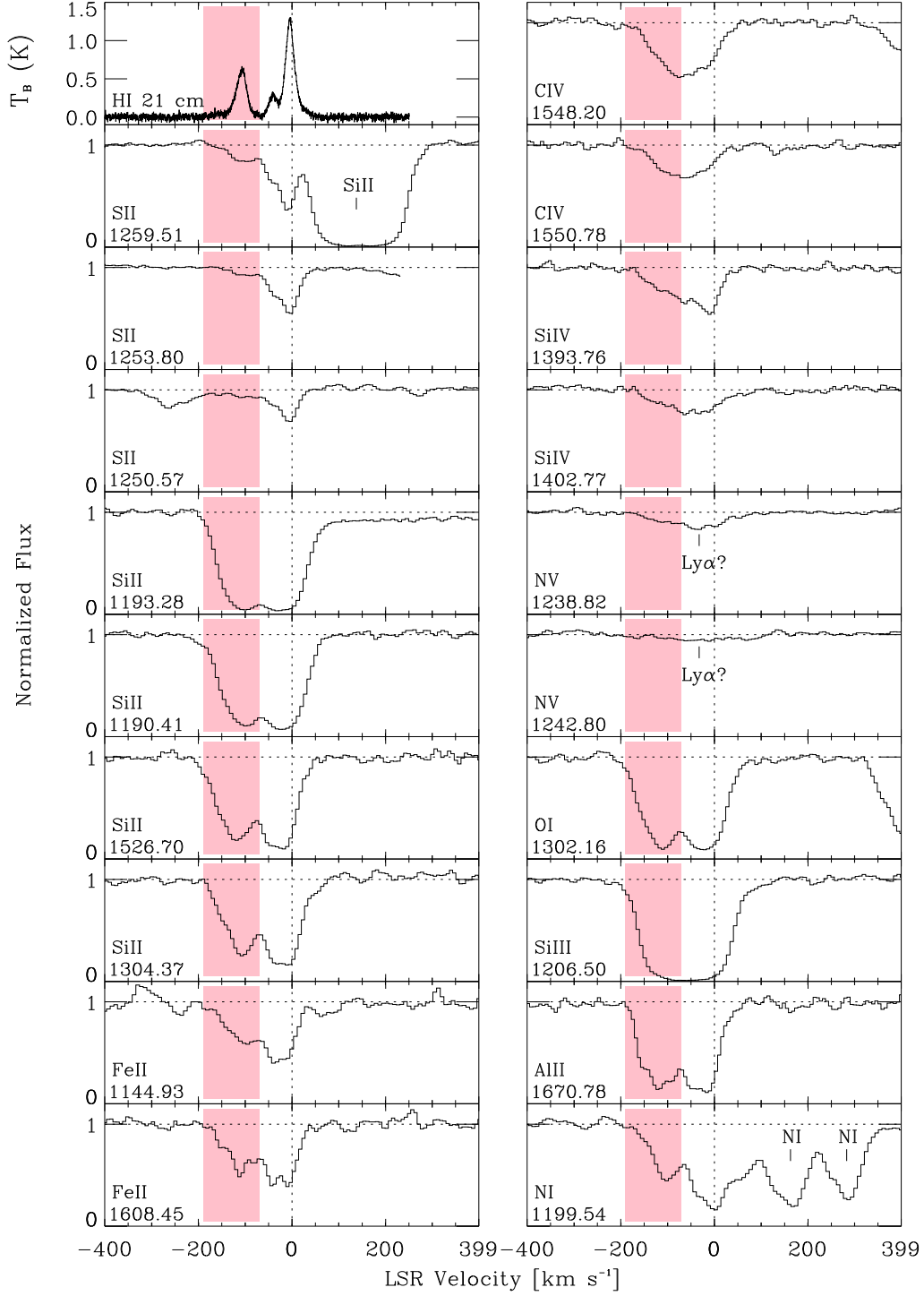


Fig. 8.— Plot of H I emission (top left panel) and UV ion absorption profiles, continuum-normalized, stacked, and aligned in velocity space for the HVC toward Mrk 817. Complex C (pink wash) appears between $V_{\text{LSR}} = -190$ and -70 km s⁻¹. IGM absorbers (Ly α) appear to contaminate both N V lines, which we treat as upper limits.

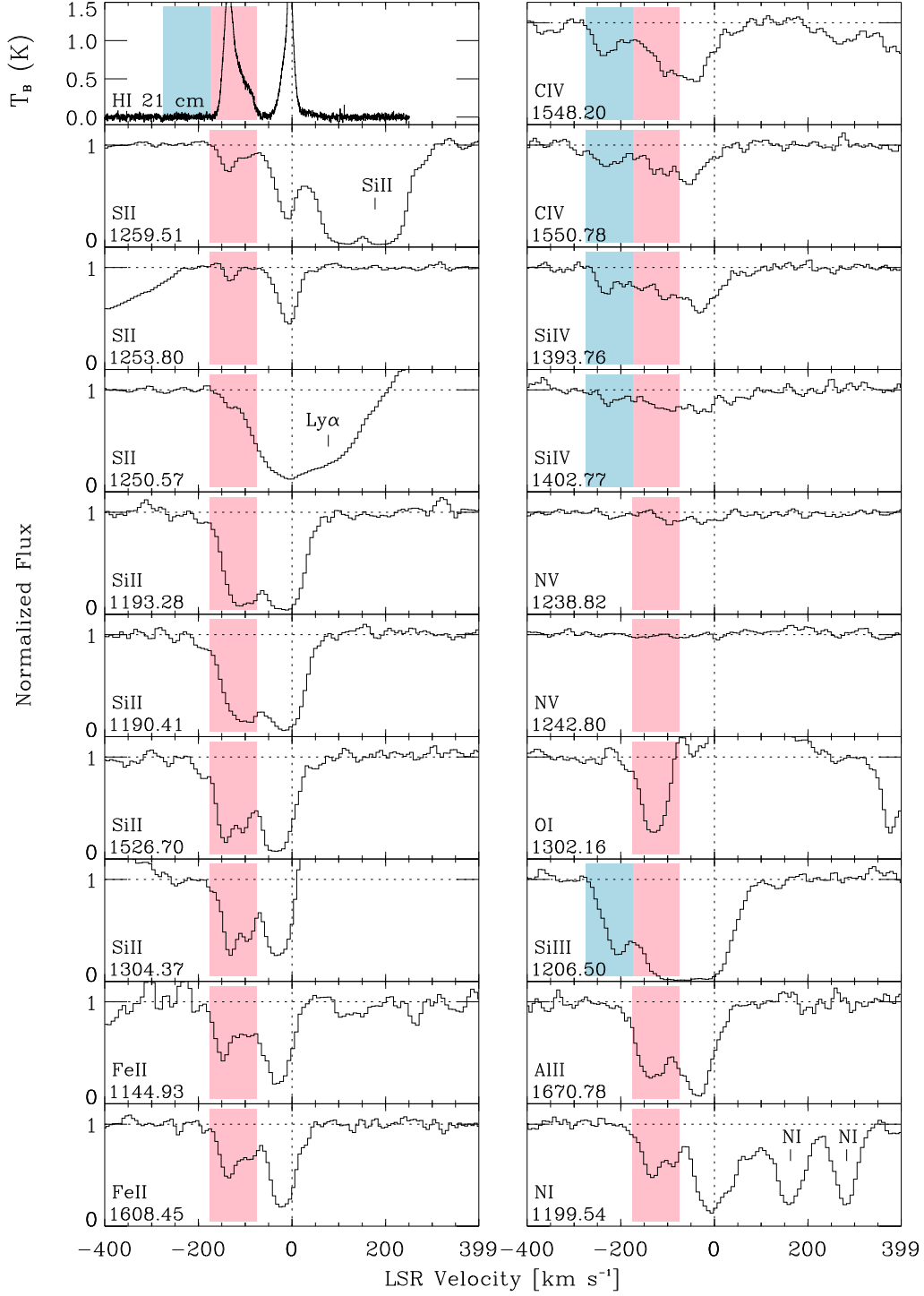


Fig. 9.— Same as Fig. 8 for two HVCs toward Mrk 290, at $\langle V_{\text{LSR}} \rangle = -120$ km s^{-1} (pink wash) and -220 km s^{-1} (blue wash). Complex C lies at $V_{\text{LSR}} = -160$ to -75 km s^{-1} . An IGM absorber (Ly α) is noted in the red wing of S II $\lambda 1250$.

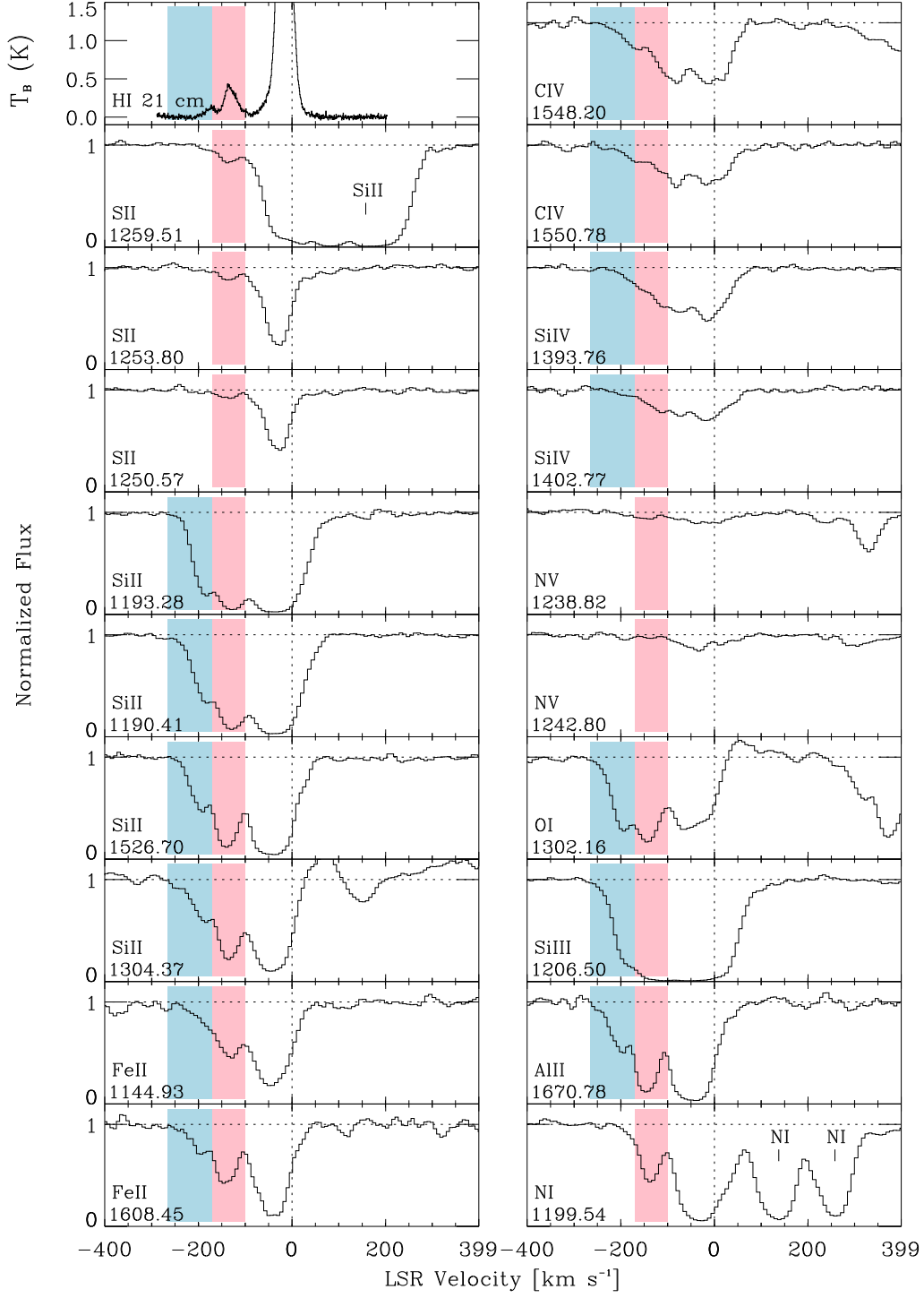


Fig. 10.— Same as Fig. 8 for HVC toward Mrk 876. We find two HVCs at $\langle V_{\text{LSR}} \rangle = -133$ km s⁻¹ (pink wash) and $\langle V_{\text{LSR}} \rangle = -190$ km s⁻¹ (blue wash).

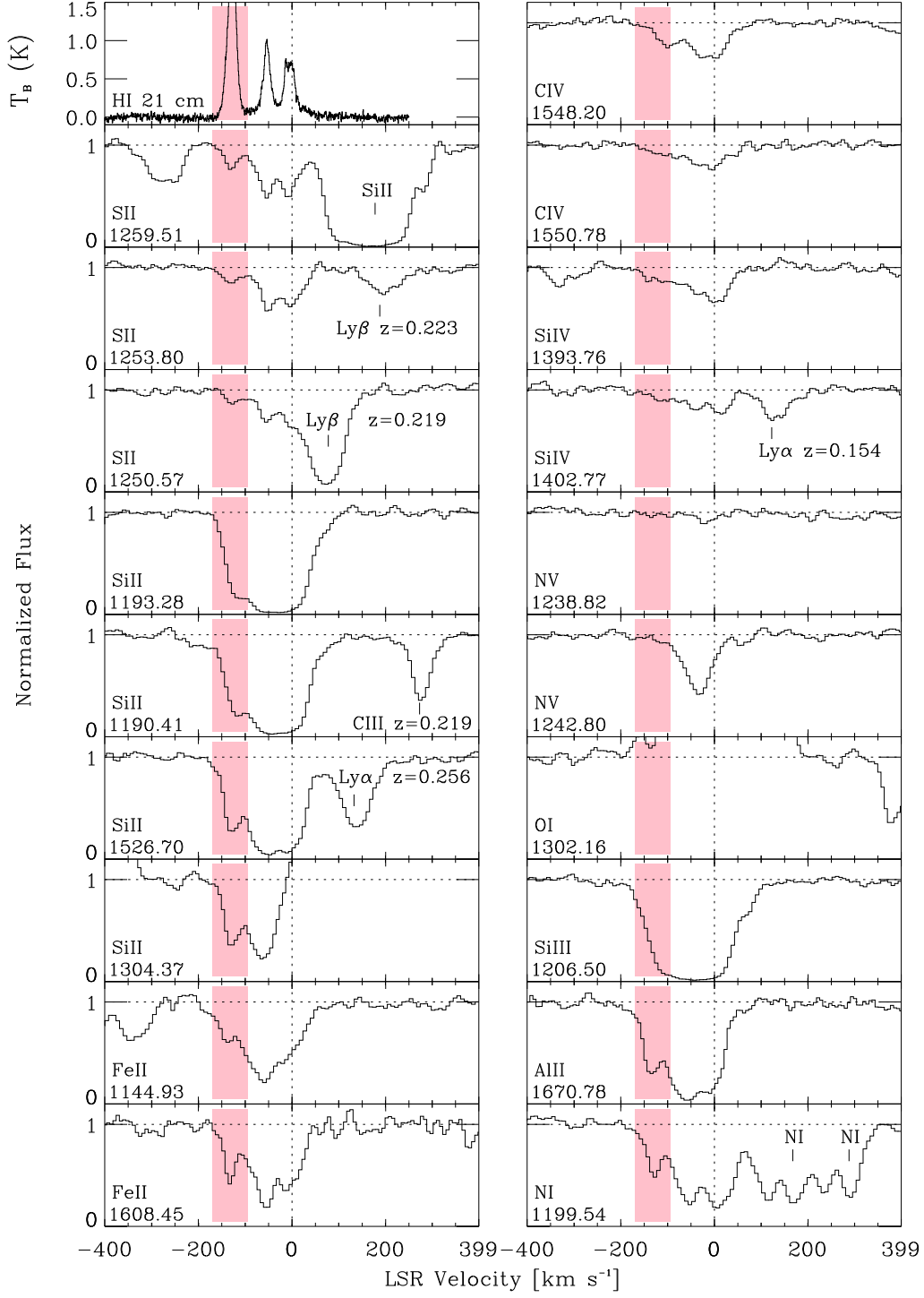


Fig. 11.— Same as Fig. 8 for HVC at $\langle V_{\text{LSR}} \rangle = -128$ km s⁻¹ (pink wash) toward PG 1259+593. IGM absorbers (Lyα, Lyβ, C III) are noted.